Monthly Notices
of the
ROYAL ASTRONOMICAL SOCIETY

MNRAS **478,** 2438–2460 (2018)
Advance Access publication 2018 May 07

doi:10.1093/mnras/sty1046

Quantifying the AGN-driven outflows in ULIRGs (QUADROS) III: measurements of the radii and kinetic powers of eight near-nuclear outflows

R. A. W. Spence,★ C. N. Tadhunter, M. Rose and J. Rodríguez Zaurín
Department of Physics and Astronomy, University of Sheffield, Sheffield S3 7RH, UK

Accepted 2018 April 16. Received 2018 March 29; in original form 2018 January 12

ABSTRACT

As part of the Quantifying ULIRG AGN-driven Outflows (QUADROS) project to quantify the impact of active galactic nuclei (AGN)-driven outflows in rapidly evolving galaxies in the local Universe, we present observations of eight nearby ultraluminous infrared galaxies (ULIRGs, $0.04 < z < 0.2$) taken with the Intermediate-dispersion Spectrograph and Imaging System on the *William Herschel Telescope* (*WHT*), and also summarize the results of the project as a whole. Consistent with Rose et al. (2018), we find that the outflow regions are compact ($0.08 < R_{[\mathrm{O\,III}]} < 1.5$ kpc), and the electron densities measured using the [S II], [O II] trans-auroral emission-line ratios are relatively high ($2.5 < \log n_{\mathrm{e}}$ (cm^{-3}) < 4.5, median $\log n_{\mathrm{e}}$ (cm^{-3}) ~ 3.1). Many of the outflow regions are also significantly reddened (median $E(B-V) \sim 0.5$). Assuming that the deprojected outflow velocities are represented by the fifth percentile velocities (v_{05}) of the broad, blueshifted components of [O III] λ5007, we calculate relatively modest mass outflow rates ($0.1 < \dot{M} < 20$ M$_\odot$ yr^{-1}, median $\dot{M} \sim 2$ M$_\odot$ yr^{-1}), and find kinetic powers as a fraction of the AGN bolometric luminosity ($\dot{F} = \dot{E}/L_{\mathrm{bol}}$) in the range $0.02 < \dot{F} < 3$ per cent (median $\dot{F} \sim 0.3$ per cent). The latter estimates are in line with the predictions of multi-stage outflow models, or single-stage models in which only a modest fraction of the initial kinetic power of the inner disc winds is transferred to the larger scale outflows. Considering the QUADROS sample as a whole, we find no clear evidence for correlations between the properties of the outflows and the bolometric luminosities of the AGN, albeit based on a sample that covers a relatively small range in L_{bol}. Overall, our results suggest that there is a significant intrinsic scatter in outflow properties of ULIRGs for a given AGN luminosity.

Key words: galaxies: active – galaxies: evolution – galaxies: kinematics and dynamics.

1 INTRODUCTION

Over the past two decades, outflows induced by active galactic nuclei (AGN) have been detected in merging galaxies across all gas phases (ionized, e.g. Rodríguez Zaurín et al. 2013; Harrison et al. 2012, 2014; neutral, e.g. Rupke, Veilleux & Sanders 2005; Morganti et al. 2016, and molecular, e.g. Spoon et al. 2013; Cicone et al. 2014; Morganti 2015). In order to reproduce the observed correlations between the central black hole (BH) and host galaxy properties, such outflows are now routinely incorporated into hydrodynamical simulations (Di Matteo, Springel & Hernquist 2005; Springel, Di Matteo & Hernquist 2005; Johansson, Burkert & Naab 2009). Results from these simulations suggest that the AGN-induced outflows have a substantial effect on the growth of galaxies. However, from an observational perspective, considerable uncertainties remain about their net impact.

In the case of warm ionized outflows, which are observed via emission lines at optical wavelengths, this uncertainty arises from a lack of accurate diagnostics of the properties of the outflowing gas. Although much recent attention has been paid to galaxies at high redshifts, which show signs of AGN activity (e.g. Nesvadba et al. 2008; Cano-Díaz et al. 2012; Harrison et al. 2012, 2014; Carniani et al. 2015, 2016; Perna et al. 2015), there is a limit to what can be learnt in detail about the co-evolution of BHs and galaxy bulges in such objects because of both their faintness, and the fact that many important diagnostic lines are shifted out of the optical/near-infrared (IR) wavelength range.

Fortunately, the hierarchical evolution of galaxies is continuing in the local Universe, albeit at a reduced rate. Ultraluminous infrared galaxies (ULIRGs: $L_{\mathrm{IR}} > 10^{12}$ L$_\odot$) (Sanders & Mirabel

★ E-mail: rspence1@sheffield.ac.uk

1996), which almost ubiquitously show signs of being involved in major mergers (i.e. tidal tails and multiple nuclei), represent local analogues of the extreme starburst galaxies detected in the distant Universe. However, they have the considerable advantage of being close enough to study in detail. Furthermore, the subset of ULIRGs with optical AGN show evidence for warm outflows in the form of broad (full width at half-maximum, FWHM $> 1000\,\mathrm{km\,s^{-1}}$) and blueshifted ($|v_{\rm out}| > 500\,\mathrm{km\,s^{-1}}$) emission lines (e.g. Spoon & Holt 2009; Rodríguez Zaurín et al. 2013; Arribas et al. 2014). However, the high degree of uncertainty in estimates of the radial extents, reddening and densities of warm outflows mean their fundamental properties (e.g. mass outflow rates and kinetic powers) have not yet been determined with any accuracy.

To address these issues, we are undertaking a programme that combines high-resolution *Hubble Space Telescope* (*HST*) imaging with wide-spectral-coverage spectroscopic observations to measure outflow properties of local ULIRGs – the Quantifying ULIRG AGN-Driven Outflows (QUADROS) project. We take advantage of a technique pioneered by Holt et al. (2011) which uses the trans-auroral [S II](4072/6725) and [OII](3727/7325) emission-line ratios to simultaneously determine the density and reddening. The full QUADROS sample, consisting of 15 objects, is described in Paper I (Rose et al. 2018), where we present deep *Very Large Telescope* (*VLT*)/Xshooter spectroscopic observations of nine objects. Paper II (Tadhunter et al. 2018) presents *HST* Advanced Camera for Surveys (ACS) imaging of eight objects with optical AGN.

In this third installment of the project, we present spectroscopy of a further seven local ULIRGs in our QUADROS sample, plus one additional ULIRG, observed with the Intermediate-dispersion Spectrograph and Imaging System (ISIS) on the *William Herschel Telescope* (*WHT*) on La Palma. Section 2 describes the sample selection, observations, and data reduction. In Section 3, we provide measurements of the radii and kinematics of the outflows. We then use the trans-auroral line ratios to estimate the electron densities and reddening, and hence derive the mass outflow rates and kinetic powers of the warm AGN-driven outflows, which we compare with those for neutral and molecular outflows in Section 4. We also investigate possible links between the warm outflows and the properties of the AGN (Section 5), and consider whether the densities determined using the high-critical-density trans-auroral emission lines are representative of the warm outflows as a whole (Section 6).

Throughout the paper, we assume a cosmology with $H_0 = 73\,\mathrm{km\,s^{-1}\,Mpc^{-1}}$, $\Omega_0 = 0.27$, and $\Omega_\Lambda = 0.73$.

2 SAMPLE SELECTION, OBSERVATIONS, AND DATA REDUCTION

2.1 The sample

The full QUADROS sample of 15 objects is a 90 per cent complete sample of local ULIRGs selected from the 1Jy sample of Kim & Sanders (1998) that show evidence for warm outflows based on their [O III] emission-line profiles (see Rose et al. 2018, for details). Most objects are classified as having type 2 Seyfert nuclei, based on the emission-line diagnostic criteria of Yuan, Kewley & Sanders (2010), have right ascensions (RA) in the range $12\,\mathrm{h} < \mathrm{RA} < 02\,\mathrm{h}$, declinations $\delta > -25^\circ$ and redshifts $z < 0.175$. However, F15462–0450 from Rose et al. (2018) is a type 1 AGN. In addition, based on the rise in the continuum at the red end of its optical spectrum (see Fig. 1), and detection of broad components to both the Hα and Paα emission lines (Veilleux, Kim & Sanders 1999; Rodríguez Zaurín et al. 2013), F23060+0505 also has a reddened type 1 AGN component.

In Paper I, Rose et al. (2018) present an analysis of seven (mostly southern) objects in the QUADROS sample, plus two additional ULIRGs, observed with *VLT*/Xshooter.

Here, we present *WHT*/ISIS observations of a further seven objects from the sample, plus one additional Seyfert ULIRG – IRAS F05189–2524 – which meets our spectral and redshift criteria, but falls outside of the RA and Dec. ranges for the QUADROS sample. This object was observed to fill a gap in the observing schedule. Note that, for the remaining ULIRG in the sample (IRAS F13428+5608), a detailed study of the off-nuclear ionized emission has been published separately (see Spence et al. 2016). The current paper will focus on the near-nuclear outflows, and F13428+5608, which was observed with only a single off-nuclear slit due to its extensive ionized nebula, will be excluded from the discussion. Two of the targets in this sample (F01004–2237 and F05189–2524) were also observed with *HST*/Space Telescope Imaging Spectrograph (STIS, long-slit spectroscopy) and four objects (F13428+5608, F14394+5332E, F17044+6720, and F17179+5444) using *HST*/ACS narrow-band imaging (see Tadhunter et al. 2018).

Table 1 shows the basic properties of the objects in the sample, and Table 2 gives details of the observations.

2.2 *WHT*/ISIS observations

Long-slit spectra for the objects considered in this paper were taken in 2014 June and 2015 September with the ISIS dual-beam spectrograph[1] on the 4.2 m *WHT* on La Palma, Spain. These observations were optimized to make accurate measurements of the trans-auroral [SII] λ4072 and [OII] λ7325 emission features, in order to facilitate estimation of the electron densities and reddening for the warm gas (Holt et al. 2011; Rose et al. 2018). We used the R300B and R316R gratings on the blue and red arms respectively, along with a dichroic cutting at 6100 Å, to achieve spectral coverage of 3600–8800 Å. This ensured that the key emission lines were contained in the spectral range that is relatively unvignetted.

Use of a 1.5 arcsec slit resulted in spectral resolutions of 5.4(5.6) $\pm$ 0.1 Å on the blue arm, and 5.1(5.4) $\pm$ 0.2(0.1) Å on the red arm for the 2014(2015) observations, as measured using the mean spectral FWHM of several prominent night-sky lines. This corresponds to $272(283) \pm 5\,\mathrm{km\,s^{-1}}$ at 5938 Å, and $222(236) \pm 9(4)\,\mathrm{km\,s^{-1}}$ at 6876 Å, for the blue and red arms respectively. In order to minimize the effects of differential atmospheric refraction, the objects were observed with the slit aligned along the parallactic angle for the centre of the observations. A 2×2 binning mode was used, resulting in a spatial scale of 0.4 arcsec pixel^{-1}, and dispersions of 1.73 and 1.84 Å on the blue and red arms, respectively. The integration time per object ranged between 2700 and 6000 s per arm. We also took observations of A-type stars at the mid-point of each set of observations in order to facilitate removal of telluric absorption features from the target spectra, as well as three spectrophotometric standard stars per night for accurate flux calibration.

Unfortunately, *WHT*/ISIS does not provide acquisition images that could be used for the calculation of the seeing. The RoboDIMM (Robotic Differential Image Motion Monitor) on La Palma does monitor the seeing each night, however it points continuously

[1] http://www.ing.iac.es/astronomy/instruments/isis

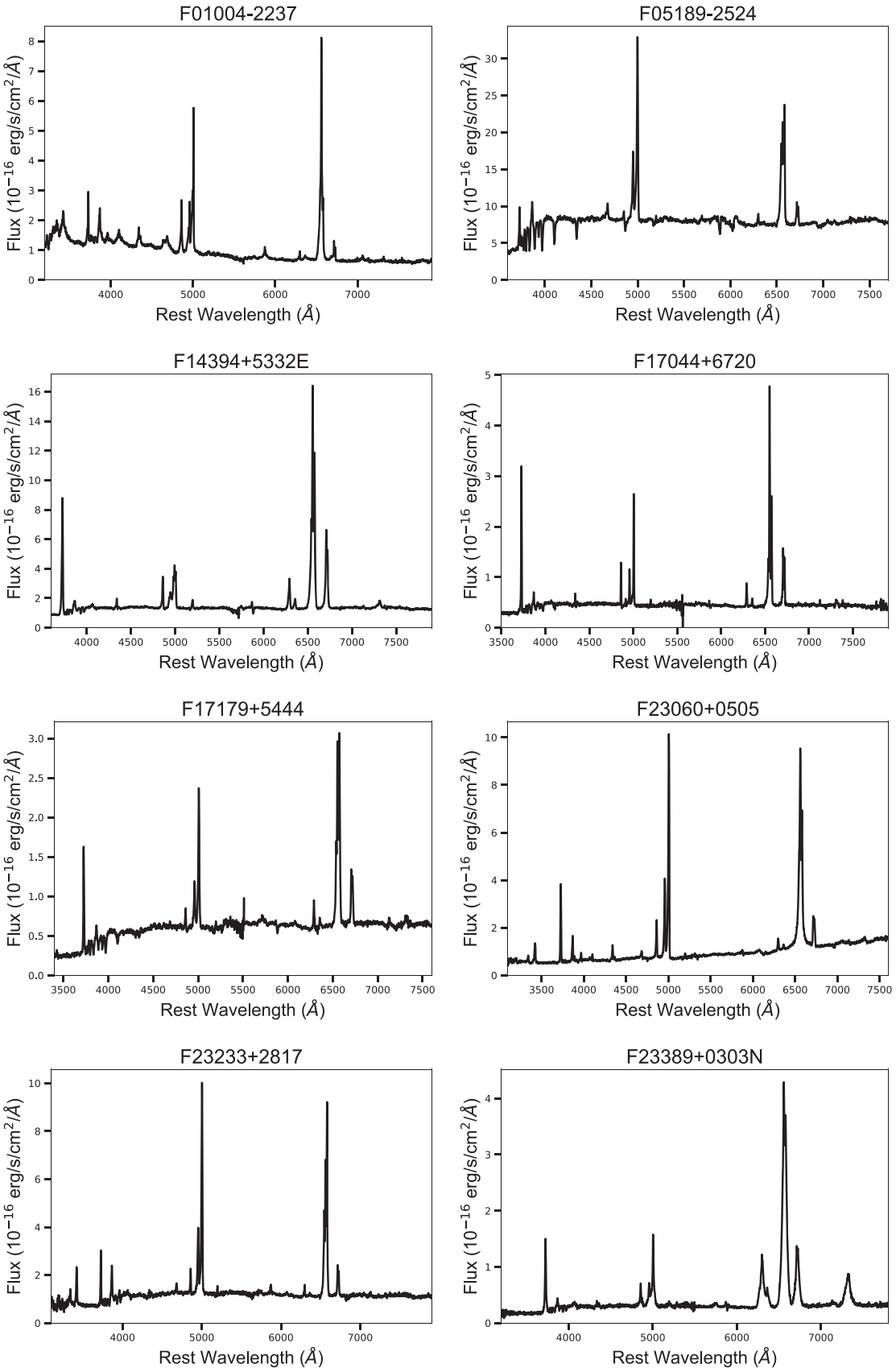

Figure 1. The rest-frame nuclear spectra for the eight ULIRGs considered in this paper.

Table 1. Properties of the ULIRGs discussed in this paper. Column (1): object designation in the IRAS Bright Galaxy Survey (BGS, Soifer et al. 1987); column (2): optical redshifts measured from the *WHT*/ISIS spectra in this paper; columns (3) and (4): right ascensions and declination of the IRAS source position as listed in the SIMBAD astronomical data base; column (5): IR luminosity; columns (6) and (7): nuclear structure and separation from Veilleux, Kim & Sanders (2002); and column (8): interaction class from Veilleux et al. (2002). Class III: pre-merger; class IV: merger; class V: old merger; Tpl: Triple; and Iso: Isolated.

Object name IRAS (1)	z (2)	RA (J2000.0) (3)	Dec. (J2000.0) (4)	log L_{IR} ($L_\odot$) (5)	Nuclear structure (6)	Nuclear separation (kpc) (7)	IC (8)
F01004–2237	0.11783 ± 0.00009	01 02 49.9	– 22 21 57	12.28	Single	–	V
F05189–2524	0.04275 ± 0.00007	05 21 01.4	– 25 21 45	12.07	Single	–	IV
F13428+5608	0.03842 ± 0.00004	13 44 42.1	+ 55 53 13	12.14	Double/multiple	0.7	IV
F14394+5332E	0.10517 ± 0.00017	14 41 04.4	+ 53 20 09	12.08	Multiple	54.0	Tpl
F17044+6720	0.13600 ± 0.00014	17 04 28.5	+ 67 16 28	12.17	Single	–	IV
F17179+5444	0.14768 ± 0.00015	17 18 54.4	+ 54 41 48	12.24	Single	–	IV
F23060+0505	0.17301 ± 0.00007	23 08 34.0	+ 05 21 29	12.48	Single	–	IV
F23233+2817	0.11446 ± 0.00010	23 25 49.4	+ 28 34 21	12.04	Single	–	Iso.
F23389+0303N	0.14515 ± 0.00013	23 41 30.3	+ 03 17 27	12.13	Double	5.2	III

Table 2. Log of the spectroscopic observations. Column (1): object designation in IRAS BGS; column (2): date of observation; column (3): position angle of the spectroscopic slit; column (4): total exposure time per arm; column (5): range of airmass during observations; and column (6): estimated 1D seeing measured from the FWHM of a telluric standard star, which was observed at the same time and with approximately the same conditions as the target. The error is deduced from the standard error on the mean of the seeing variation over the observation period, as measured by the RoboDIMM. Column (7): Galactic extinction in A_V from Schlafly & Finkbeiner (2011). Column (8): the size of the nuclear extraction aperture in kpc. Column (9): scale in kpc for 1 arcsec at the redshift of the galaxy.

Object name IRAS (1)	Date (2)	PA (deg) (3)	Integration (s) (4)	Airmass (5)	$Seeing_{1D}$ FWHM (arcsec) (6)	GA_V (mag.) (7)	Aperture (kpc) (8)	Scale (kpc $arcsec^{-1}$) (9)
	09/2015	5	6000	1.59–1.68	1.43 ± 0.12	0.048	4.9	2.033
F01004−2237								
	09/2015	340	2700	1.83–1.98	1.63 ± 0.05	0.080	4.8	0.808
F05189−2524								
F13428+5608	06/2014	23	3000	1.15–1.19	1.20 ± 0.35	0.022	–	–
	06/2014	130	6000	1.13–1.30	1.25 ± 0.07	0.031	5.2	1.849
F14394+5332E								
F17044+6720	06/2014	145	6000	1.29–1.40	1.61 ± 0.07	0.081	4.6	2.300
F17179+5444	06/2014	105	6000	1.25–1.57	1.60 ± 0.06	0.082	4.9	2.471
F23060+0505	09/2015	325	5400	1.11–1.28	1.07 ± 0.11	0.173	5.6	2.813
F23233+2817	09/2015	282	6000	1.28–1.83	1.17 ± 0.15	0.331	4.7	1.972
	09/2015	0	5400	1.11–1.14	1.44 ± 0.10	0.145	4.9	2.427
F23389+0303N								

towards stars close to the zenith and so is not accurate for the positions of our individual objects. Instead, we have used the spatial FWHM of the telluric standard stars, as measured from our long-slit observations, to estimate the seeing for each object.

To do this, we extracted spatial slices across a ∼ 10 Å wavelength range close to the wavelengths of the redshifted [OIII] λ5007 in the 2D spectra of the telluric stars, and fit a single Gaussian to the resultant 1D profiles using DIPSO. This technique has the advantage over 2D DIMM seeing estimates in that it accounts for the integration of the seeing disc across the spectroscopic slit (see the discussion in Rose et al. 2018). The 1D seeing (FWHM) estimates obtained in this way ranged from 1.07 to 1.63 arcsec across the two nights of observations. The estimates for the individual objects are displayed in Table 2.

Note that the exposure times for the telluric standard stars were short compared with those of the science targets, so the errors on the 1D Gaussian fits to the telluric star profiles underestimate the true uncertainty on the seeing, which is likely to be dominated by seeing variations over the whole observation period for each target. Therefore, we used the RoboDIMM measurements – taken every 2 min – to provide an estimate of the likely variation in the seeing over the observation period, and use the standard error on the mean of the RoboDIMM measurements as a more realistic estimate of the uncertainty in the seeing.

2.2.1 *Data reduction*

The data were reduced (bias-subtracted, flat-field corrected, cleaned of cosmic rays, wavelength calibrated, and flux calibrated) and straightened before extraction of the individual spectra using standard packages in IRAF, and the STARLINK packages FIGARO and DIPSO. The wavelength calibration accuracy, determined using the mean shift between the published[2] and measured wavelengths of night-sky emission lines, was ∼0.5(0.2) Å and ∼0.5(0.3) Å for the 2014 (2015) blue and red arms, respectively. The estimated uncertainty for the relative flux calibration across the full spectral range of the observations was ±5 per cent, based on the comparison of the

[2]http://www.eso.org/observing/dfo/quality/UVES/txt/sky/

response curves of the three spectrophotometric standard stars observed in each run. An important detail to note is that the pixel scales of the blue and red arms of ISIS are different (0.4 and 0.44 arcsec, respectively). This was corrected using the ISTRETCH command within FIGARO, resulting in a common pixel scale of 0.4 arcsec across both arms. The data from the red arm were also corrected for telluric absorption features using the A-type stars observed at similar time and airmass as each science target.

2.2.2 *Aperture extraction*

The ULIRGs in this sample are known to exhibit strong AGN-induced outflows (Rodríguez Zaurín et al. 2013) that are concentrated in their nuclear regions. Therefore, we used extraction apertures of ∼5 kpc diameter centred on the nuclei, as in Rodríguez Zaurín, Tadhunter & González Delgado (2009). Using the pixel scale of the CCD and the cosmology-derived arcsecond-to-kpc conversion factors, 5 ± 0.6 kpc apertures were extracted for all objects (see Table 2, column 8). This resulted in eight nuclear spectra for analysis, which are shown in Fig. 1. In the following sections, we describe the results obtained by fitting the profiles of the emission lines detected in these nuclear spectra. It should be noted that the quality of the data in the vicinity (within ∼100 Å) of the dichroic cut at ∼6100 Å (observed frame) is relatively poor. Fortunately, this does not affect any of our key diagnostic emission lines.

2.3 *HST*/STIS observations

In addition to the *WHT*/ISIS spectroscopy, we also used spectral data taken with the Space Telescope Imaging Spectrograph (STIS) – installed on the *HST* – to provide additional information on the spatial extents and physical conditions of the outflows. *HST*/STIS observations were available for two of the ULIRGS in this paper: F01004–2237 and F05189–2524 (Farrah et al. 2005). These space-based observations have the advantage of higher spatial resolution, and the narrow slit reduces the level of stellar contamination from the host galaxy, which otherwise reduces the equivalent widths of the weaker trans-auroral lines in the ground-based spectra.

Both objects were observed using the G430L and G750L gratings with the 52 × 0.2 arcsec slit. The main spectroscopic reduction steps were performed by the Space Telescope Science Institute STIS pipeline *calstis*. As in Rose et al. (2018), we then used IRAF and STARLINK packages to improve the bad pixel and cosmic ray removal.

2.4 Fitting the emission-line profiles

Our fitting technique is described in detail in Rose et al. (2018); however, for completeness we provide an overview here.

Prior to modelling the emission-line profiles, the spectra were corrected for Galactic extinction using the extinction function of Cardelli, Clayton & Mathis (1989) and *E(B-V)* values from Schlafly & Finkbeiner (2011). They were then shifted to the galaxy rest frame using redshifts measured from the higher order Balmer stellar absorption features (3798, 3771, and 3750 Å where possible). One exception to this is F01004–2237, for which strong non-stellar continuum emission dominates over the stellar absorption features. In this case, the rest frame was estimated using four narrow off-nuclear emission lines detected in kinematically quiescent regions extending ∼10 arcsec (∼20 kpc) either side of the nucleus. The redshifts and their associated errors are given in Table 1.

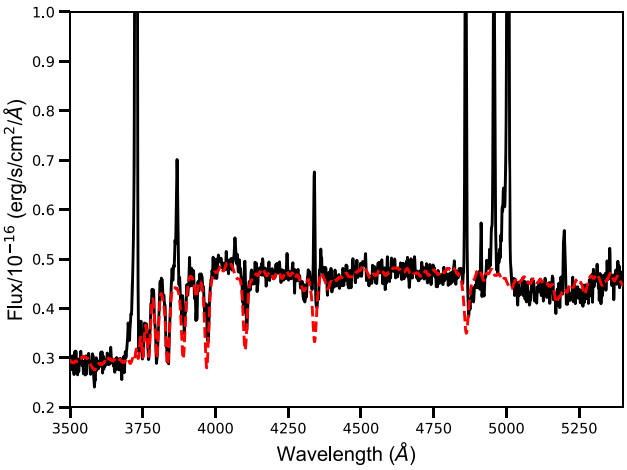

Figure 2. The nuclear spectrum of F17044+6720 (black, solid line), overplotted with the STARLIGHT fit to the stellar continuum (red, dashed line).

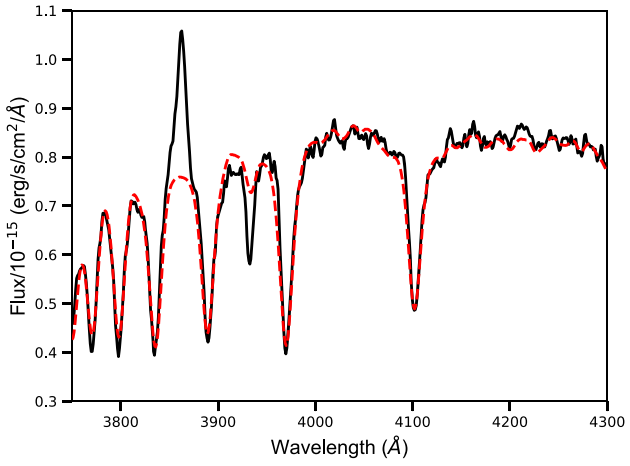

Figure 3. A zoom-in on the higher order Balmer absorption features (Hδ–H11) in the nuclear spectrum of F05189–2524. Also shown is the [NeIII] emission line at 3869 Å and the CaII K ISM absorption feature at 3933 Å. The black solid line represents the data, and the red dashed line shows the STARLIGHT fit.

The spectra of six objects were then fitted with the spectral synthesis code STARLIGHT (Cid Fernandes et al. 2005), using the Bruzual & Charlot (2003, BC03) solar metallicity base templates in order to facilitate accurate stellar continuum subtraction. The fit to the full optical spectrum of F17044+6720 is shown in Fig. 2, for reference. A zoom on the part of the spectrum containing the Balmer absorption lines of F05189−2524 is also provided in Fig. 3, illustrating the excellent consistency of the STARLIGHT fit with the estimated redshift and the stellar absorption line profiles. Note that no attempt was made to fit F01004−2237. The continuum of this object is highly complex due to the fact that its spectrum is dominated by the emission of a recent tidal disruption event (TDE; Tadhunter et al. 2017). Similarly, STARLIGHT struggled to fit the continuum in the red arm of F23060+0505 due to an underlying reddened type 1 AGN component. Therefore, we did not remove the stellar continua in these cases.

The [O III] λ5007 emission line is the strongest and cleanest high-ionization line associated with the outflowing ionized gas. For this

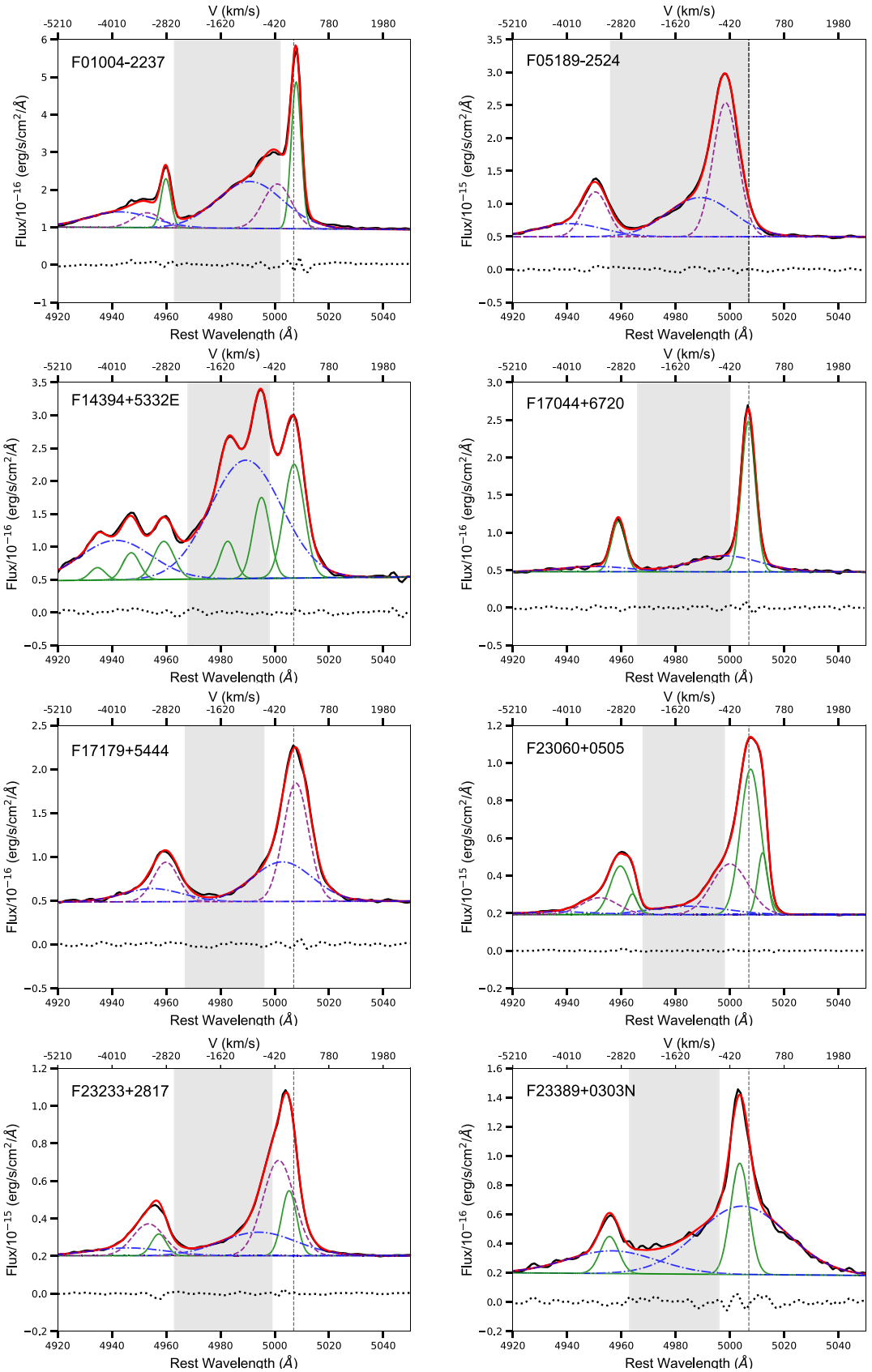

Figure 4. [O III] profiles and fits for all ULIRGS considered in this paper. The black solid line represents the data, and the overall fit is shown by the red solid line. The individual components are coloured as follows: narrow (green, solid); intermediate (purple, dashed); and broad (blue, dot–dashed). The residuals of the fits are shown below the profiles (black, dashed). The shaded regions show the velocity ranges extracted when determining the outflow radii.

Table 3. The [O III] kinematics for the ULIRGs considered in this paper. Columns (3) and (4) give the FWHM and velocity shift of each component. Columns (5) and (6) indicate whether the [O III] kinematic model worked for the H α+[N II], [O II], and [S II] blends. Columns (7) and (8) give the observed [O III] λ5007 and H β fluxes associated with each kinematic component.

Object IRAS (1)	Component (2)	FWHM (km s^{-1}) (3)	ΔV (km s^{-1}) (4)	H α + [N II] (Y/N) (5)	[O II]/[S II] (Y/N) (6)	[O III] λ5007 flux (erg s^{-1} cm^{-2}) (7)	H β flux (erg s^{-1} cm^{-2}) (8)
F01004−2237	N	Unresolved	63 ± 25	N	N	(2.03 ± 0.04)E−15	(4.71 ± 0.02)E−16
	I	699 ± 32	− 361 ± 35			(1.99 ± 0.14)E−15	(6.10 ± 0.09)E−16
	B	1586 ± 38	− 1045 ± 60			(3.68 ± 0.16)E−15	(1.55 ± 0.10)E−15
F05189−2524	I	582 ± 37	− 505 ± 26	N	N	(2.48 ± 0.04)E−14	(1.93 ± 0.14)E−15
	B	1706 ± 24	− 1072 ± 44			(1.91 ± 0.05)E−14	(1.09 ± 0.12)E−15
	$I_{H\beta}$	555 ± 76	− 28 ± 55			–	(1.53 ± 0.21)E−15
F14394+5332E	N1	408 ± 11	17 ± 62	N	N	(1.61 ± 0.03)E−15	–
	N2	288 ± 21	− 701 ± 63			(9.01 ± 0.44)E−16	–
	N3	242 ± 34	− 1457 ± 66			(4.00 ± 0.32)E−16	–
	B	1871 ± 19	− 1000 ± 67			(7.02 ± 0.10)E−15	–
	$N_{H\beta}$	420 ± 11	17 ± 63			–	(2.08 ± 0.06)E−15
	$I_{H\beta}$	986 ± 42	− 358 ± 93			–	(1.05 ± 0.07)E−15
	$B_{H\beta}$	1927 ± 20	− 1030 ± 69			–	(5.42 ± 0.52)E−16
F17044+6720	N	218 ± 12	− 1 ± 61	Y	Y	(1.46 ± 0.01)E−15	(6.61 ± 0.10)E−16
	B	1757 ± 60	− 503 ± 85			(7.64 ± 0.33)E−16	(1.58 ± 0.24)E−16
F17179+5444	I	590 ± 12	58 ± 62	Y	Y[a]	(1.81 ± 0.04)E−15	(4.12 ± 0.18)E−16
	B	1530 ± 33	− 242 ± 78			(1.43 ± 0.05)E−15	(2.20 ± 0.27)E−16
F23060+0505[b]	N1	147 ± 37	273 ± 34	Y[c]	N	(4.09 ± 0.45)E−15	(6.94 ± 0.87)E−16
	N2	267 ± 35	− 25 ± 38			(4.76 ± 0.49)E−15	(9.60 ± 1.02)E−16
	I	934 ± 32	− 283 ± 44			(6.94 ± 0.28)E−15	(8.07 ± 0.59)E−16
	B	1399 ± 114	− 1220 ± 146			(1.62 ± 0.30)E−15	–
	$BLR_{H\alpha}$	2359 ± 69	393 ± 102			–	–
F23233+2817	N	239 ± 21	− 92 ± 27	Y	Y[d]	(2.56 ± 0.14)E−15	(6.50 ± 0.58)E−16
	I	760 ± 13	− 316 ± 31			(8.35 ± 0.22)E−15	(6.61 ± 0.92)E−16
	B	1892 ± 40	− 785 ± 54			(4.71 ± 0.19)E−15	(4.52 ± 0.98)E−16
	N	402 ± 16	− 191 ± 27	Y	Y	(7.80 ± 0.20)E−16	(3.60 ± 0.13)E−16
F23389+0303N							
	VB	2346 ± 38	− 134 ± 36			(2.26 ± 0.25)E−15	(7.81 ± 0.25)E−16

Notes. [a]The [O III] model worked for the trans-auroral [O II] blend, but not for the [S II]. In this case, a two-component model with different widths and shifts was required for the strong blend. The broad component to the weak trans-auroral [S II] blend was not detected.
[b]H β was fit with just narrow and intermediate components. No broad component was required.
[c]The [N II] lines were well fit with the [O III] model. H α was fit with the narrow and intermediate components of the [O III] model, however the broad component was dominated by a BLR component (FWHM > 2000 km s^{-1}).
[d]The [S II] blends did not require a broad component.

reason, we first concentrated our emission-line fitting procedure on this line. Our approach was to fit the line profile with the minimum number of Gaussians required to give an acceptable fit. We constrained the fits as much as possible, setting the relative shifts between each component of [OIII] $\lambda\lambda$4959,5007 to be 47.92 Å, and fixing the relative intensities according to those from atomic physics (1:2.99). At least two Gaussian components were required in all cases. The [O III] fits are shown in Fig. 4, along with their residuals. The velocity shifts and widths for each required component are shown in Table 3. The velocity shifts have been corrected in quadrature for the spectral resolution. For consistency, we label our components based on the line widths (FWHM) following Rodríguez Zaurín et al. (2013):

(i) narrow (N): FWHM < 500 km s^{-1};
(ii) intermediate (I): 500 < FWHM < 1000 km s^{-1};
(iii) broad (B): 1000 < FWHM < 2000 km s^{-1};
(iv) very broad (VB): FWHM > 2000 km s^{-1}.

We then attempted to apply this [O III] kinematic model (i.e. relative width and shift with respect to the rest frame for each component) to our other diagnostic emission lines ([OII] λ3727, [S II] $\lambda\lambda$4068,4076, H β, [O I] λ6300, H α, [N II] $\lambda\lambda$6548,6583, [S II] $\lambda\lambda$6716,6731, and [OII] $\lambda\lambda$7319,7331). Note that the use of the various diagnostic emission-line ratios in the following analyses requires the assumption that the flux of all of these emission lines originates from the same volume of gas. We show this assumption to be valid in Section 6.

The kinematic components were constrained according to atomic physics as follows (see also Rose et al. 2018).

(i) The [S II](4068/4076) ratios were forced to fall within the range 3.01 < [S II](4068/4076) < 3.28.
(ii) The [O II](7319/7331) ratios were fixed at 1.24.
(iii) The [N II](6583/6548) ratios were fixed at 2.99.
(iv) Where necessary, the ratios of the broad components of [S II](6717/6731) were fixed to the high-density limit value of 0.44 to ensure a physical fit.

The [O III] models were successful for the majority of emission lines in 50 per cent of our objects. An example of the application of the [O III] model fits to all the emission lines for F23389+0303N is shown in Fig. 5.

For F01004–2237, F05189–2524, F14394+5332E, and F23060+0505, the [OIII] model did not work for the other lines, and

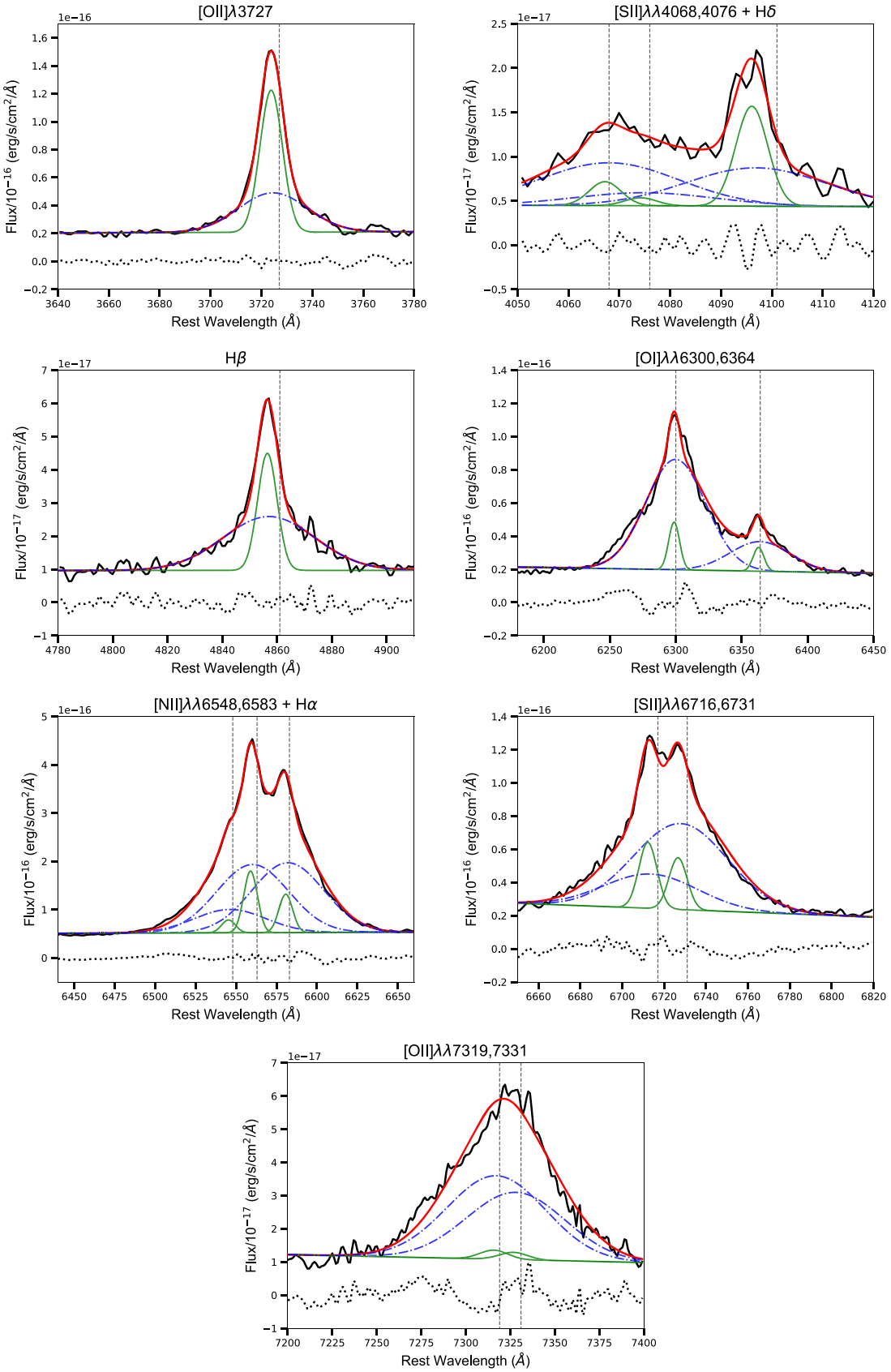

Figure 5. Emission-line profiles and fits for all diagnostic lines for F23389+0303N. The black solid line represents the data, and the overall fit is shown by the red solid line. The individual components are coloured as follows: narrow (green, solid); intermediate (purple, dashed); and broad (blue, dot–dashed). The residuals of the fit are shown below the profiles (black, dashed).

an alternative kinematic model was generated using [O II] λ3727, or [S II] λλ6716,6731 in the case of F14394+5332E.

F01004–2237, as mentioned above, appears to have recently undergone a TDE, strongly affecting its nuclear spectrum. While the three-component [OIII] model works for H β, the H α + [N II] blend only requires a two-component fit to each line, with the [NII] narrow components very weak in this case. A two-component model (narrow + broad) was required to fit the [O II] λ3727 and [S II] λ6725 blends. Note that, although the red trans-auroral [O II] λλ7319,7331 blend was detected in the *WHT*/ISIS spectrum, the blue trans-auroral [SII] λλ4068,4076 blend was not detected due to severe contamination by TDE-related emission lines. It was, however, detected in the pre-TDE *HST*/STIS spectrum of F01004–2237. Therefore, given that there is good evidence that the slit losses for the *HST*/STIS and *WHT*/ISIS spectra were similar (Tadhunter et al. 2017), the density and reddening estimates presented in Section 3.2 for this source are based on comparing the total fluxes of the blue [S II] blend measured from the *HST*/STIS spectrum (single Gaussian fit) with those of the blue [OII], red [O II] (single Gaussian fit), and red [SII] blends measured from the *WHT*/ISIS spectrum.

In the case of F05189–2524, the full [O III] λλ4959,5007 profile is blueshifted by more than 500 km s^{-1} relative to the stellar rest frame, similar to the cases of PKS1549–79 (Tadhunter et al. 2001) and F15130–1958 (Rose et al. 2018). This behaviour is also seen to a lesser extent in F23233+2817 and F23389+0303N. However, for F05189–2524, an additional rest-frame intermediate component was required for the Balmer, [O I], [O II], and [SII] emission lines in the ground-based *WHT* spectrum. Although the blueshifted intermediate and broad components were also detected in H β, the broad component was not detected in the [O I], [O II], and [SII] lines which were fitted with a two-component model consisting of a rest-frame intermediate and a blueshifted intermediate component.

In the STIS spectrum of F05189–2524, only a single Gaussian could be fitted to the trans-auroral [O II] and [S II] lines to estimate the total emission-line flux. However, the relative shift of this component is within 3σ of the blueshifted intermediate component detected in the red [S II] and blue [O II] emission lines in the ground-based spectrum. It is therefore reasonable to assume that, due to the narrower slit used for the STIS observations, the measured total flux samples the blueshifted gas within the outflow.

The [O III] profile of F14394+5332E is complex, requiring three narrow components (one rest frame, and two blueshifted) and a broad component (see also Rodríguez Zaurín et al. 2013). However, the two blueshifted narrow [O III] lines were not detected in any of the other emission lines in this object. These were instead fitted with a three-component model (one narrow, one intermediate, and one broad component), with the exception of the [NII] doublet where no broad component was required. This is likely due to degeneracy with the broad component of H α.

Finally, the [O III] profile of F23060+0505 required four components: two narrow, an intermediate, and a broad. No broad component was detected in H β, nor for the [O I] and [O II] emission lines; and only the narrow components were detected in the [S II] blends, perhaps leading to an underestimation of the outflow density for this object using the trans-auroral line ratios (Section 3.2). However, a broad-line region (BLR) component (FWHM $= 2356 \pm 69$ km s^{-1}) was required in this case to fit the H α+[N II] blend. As discussed by Rodríguez Zaurín et al. (2013), the presence of a moderately reddened type 1 AGN component in this source is confirmed by the relatively red shape of the long-wavelength end of its optical continuum spectrum (see Fig. 1), and the detection of a broad Pα emission line at near-IR wavelengths (Veilleux, Sanders & Kim 1997).

3 OUTFLOW PROPERTIES

The ultimate aim of this series of papers is to better quantify the key properties of the AGN-induced outflows in the nuclear regions of local ULIRGs. The necessary calculations require accurate determinations of the outflow kinematics, radii, electron densities, and intrinsic reddening. In this section, we present the results of our emission-line fitting.

3.1 Emission-line kinematics and outflow radii

First, we measured the kinematics and radii of the nuclear outflows. Table 3 gives the velocity shifts and widths for the required components of the [O III] λ5007 emission line, using the fitting approach described in Section 2.4. Blueshifted intermediate/broad components were detected in all objects, indicating the presence of ionized nuclear outflows, consistent with the results of (Rodríguez Zaurín et al. 2013). We concentrated our analyses on the properties of these outflowing components.

In order to properly quantify the outflow powers, it is also important to estimate their spatial extents along the slit. Currently, the true radial extents of AGN-induced outflows ($R_{\rm out}$) in luminous type 2 AGN are highly uncertain, with $R_{\rm out}$ measurements ranging from just 0.06 kpc (Tadhunter et al. 2018) to >10 kpc (Harrison et al. 2012).

To determine the radial extents in our ULIRG sample, we first isolated the outflowing (broad and blueshifted) components of the [OIII] emission line. Guided by the Gaussian fits to the emission-line profiles, we extracted spatial slices between the 95$^{\rm th}$ percentile (v_{95}) of the narrow [O III] λ4959 component fit and 5$^{\rm th}$ percentile (v_{05}) of the narrow [O III] λ5007 component fit. In this way, we sampled *only* the outflowing components, and avoided any significant narrow-line flux not associated with the outflow. In the case of F05189−2524, all components of [OIII] are significantly blueshifted with respect to the stellar rest frame. For this target, we extracted all of the [OIII] λ5007 flux blueward of the rest-frame wavelength. The velocity ranges over which the spatial profiles were extracted are given in Table 4, column 2, and indicated visually by the shaded regions in Fig. 4.

The continuum was then removed by subtracting an average continuum profile created from two ∼30 Å spatial slices, one taken blueward and the other redward of the [OIII] λλ4959,5007 blend. The resultant spatial profile was then fitted with a Gaussian. In all cases, a single Gaussian was sufficient. To assess whether we resolve the outflow, the FWHM of this spatial profile was compared to that of the estimated 1D seeing. The outflow was considered spatially resolved if the difference between the measured spatial FWHM and the 1D seeing FWHM was greater than three times the estimated uncertainty in the difference (i.e. 3σ).

In the spatially resolved cases, the 1D seeing FWHM was subtracted from the spatial FWHM in quadrature, converted to kpc using the pixel scale and angular scale on the sky consistent with our assumed cosmology, and then halved to find the radius. See section 3.1 in Rose et al. (2018) for a full discussion of this technique.

Using the ground-based spectroscopy, the outflow regions are spatially resolved for three objects, with the other objects unresolved compared to the seeing. In the latter cases, the quoted radii are upper limits, derived by calculating the radius (FWHM$_{\rm [O\,III]}$) at which the outflow would have been significantly resolved at the 3σ level

Table 4. Radial extent of the broad, outflowing [O III] λ5007 gas. Column (2): the velocity range over which the spatial slice was extracted. Columns (3) and (4) give the spatial FWHM for the outflowing and 1D seeing (extracted from a standard star over the same wavelength range), respectively. Column (6) shows the calculated outflow radii using the *WHT*, and columns (7) and (8) show the radii measured using *HST* observations for comparison.

Object name IRAS (1)	[O III] λ5007 range (km s^{-1}) (2)	FWHM$_{[O\,III]}$ (arcsec) (3)	FWHM$_{1D}$ (arcsec) (4)	Resolved *WHT*? (Y/N) (5)	R$_{[O\,III]}$ (kpc) *WHT*/ISIS (6)	*HST*/STIS (7)	*HST*/ACS (8)
F01004–2237	−2591 to −278	1.623 ± 0.017	1.430 ± 0.123	N	<1.1	0.111 ± 0.004	–
F05189–2524[a]	−3016 to 0	1.774 ± 0.014	1.634 ± 0.052	N	<0.3	0.079 ± 0.002	–
F14394+5332E	−2315 to −524	1.489 ± 0.010	1.248 ± 0.073	Y	0.75 ± 0.12	–	0.840 ± 0.008[b]
F17044+6720	−2453 to −422	2.044 ± 0.047	1.610 ± 0.069	Y	1.45 ± 0.18	–	1.184 ± 0.006
F17179+5444	−2327 to −614	1.796 ± 0.046	1.600 ± 0.060	N	<1.0	–	0.112 ± 0.007
F23060+0505	−2375 to −524	1.469 ± 0.022	1.073 ± 0.110	Y	1.41 ± 0.19	–	–
F23233+2817	−2609 to −446	1.485 ± 0.014	1.167 ± 0.154	N	<1.1	–	–
F23389+0303N	−2603 to −655	1.542 ± 0.018	1.441 ± 0.100	N	<1.2	–	–

Notes.[a]The entire [O III] λλ5007,4959 profile for this component is blueshifted by >500 km s^{-1} i.e. only the outflowing component has been detected, so the spatial profile is extracted over the entire velocity range of [O III] λ5007 blueward of the rest frame.
[b]Note that the *HST*/ACS measurement assumes that the AGN is located in the dust lane that bisects the eastern nucleus of the system.

compared to the 1D seeing (FWHM$_{1D}$):

$$\mathrm{FWHM}_{[O\,III]} < \sqrt{(\mathrm{FWHM}_{1D} + 3\sigma)^2 - (\mathrm{FWHM}_{1D})^2}. \quad (1)$$

Table 4 gives the FWHM for the spatial [O III] and 1D seeing profiles for each object (columns 3 and 4), along with the estimated radii (columns 6–8).

Two objects (F01004–2237 and F05189–2524) have space-based STIS spectroscopy available for comparison (column 7). Using the same spatial extraction technique, but considering the line spread function instead of atmospheric seeing, we calculated additional estimates for the outflow radii (see Rose et al. 2018). The radii for both objects are relatively small, consistent with the *WHT*/ISIS upper limits.

Estimates of the outflow radii for a further three objects (F14394+5332E, F17044+6720, and F17179+5444) are also available from *HST*/ACS narrow-band imaging, presented in Tadhunter et al. (2018). The *HST*-based flux-weighted mean radius estimates are given in column 8. There is remarkable consistency between the *HST*/ACS estimates and the resolved *WHT*/ISIS estimates for F14374+5332E and F17044+6720. The ACS imaging estimate for F17179+5444 is also consistent with the upper limit from the *WHT* spectroscopy.

Note that, while we can only determine an upper limit on the outflow radius for F23389+0303N leading to lower limits on the mass outflow rates and kinetic powers in this case, we also provide estimates of the outflow properties based on the radius of the radio lobes ($r = 0.415$ kpc) from Nagar et al. (2003). Although this involves the assumption that the outflows are jet-driven in this object, generally the emission-line outflows associated with compact radio sources of similar power to F23389+0303N are found to be cospatial with the radio sources (e.g. Batcheldor et al. 2007; Tadhunter et al. 2014, Tadhunter et al. in preparation).

Overall, consistent with the results of Rose et al. (2018) and Tadhunter et al. (2018), the outflows in our sample of ULIRGs are compact, with all radius estimates in the range $0.08 < R_{out} < 1.5$ kpc.

3.2 Electron density and reddening

Next, we calculated the electron densities and intrinsic reddenings of the outflows. As discussed in Rose et al. (2018), previous attempts to calculate mass outflow rates and kinematic powers in AGN have been severely limited by the lack of accurate estimates of the electron density. For AGN, the most commonly used optical diagnostics are the [S II] λλ6716, 6731 and [O II] λλ3726, 3729 doublet ratios. However, these are only sensitive to relatively low densities ($10^2 < n_e < 10^{3.5}$ cm^{-3}) and are therefore ineffective for the higher density clouds that are also expected to be associated with outflows. Furthermore, the highly blue- or redshifted, broad components associated with outflows can cause degeneracies in the fitting, due to severe blending of the emission-line profiles. These degeneracies can also affect the Hα + [NII] blend, leading to significant uncertainties in the intrinsic reddening calculated from the Balmer decrement.

For this reason, we have obtained spectra optimized for the trans-auroral [SII] λλ4068,4076 and [O II] λλ7319,7331 features. We combined these emission-line fluxes with the [SII] λλ6716, 6731 and [O II] λλ3726, 3729 fluxes as follows:

$$\mathrm{TR}([O\,II]) = F(3726 + 3729)/F(7319 + 7331); \text{ and} \quad (2)$$

$$\mathrm{TR}([S\,II]) = F(4068 + 4076)/F(6716 + 6731). \quad (3)$$

Combining the fluxes in this way gives a density diagnostic that does not suffer from the problems with degeneracies that affect the [S II](6716/6731) and [O II](3726/3729) diagnostics. This is because we are comparing the total fluxes of the widely separated blends, rather than the fluxes of the individual components within them. This technique, introduced by Holt et al. (2011), is also sensitive to a higher range of densities ($10^2 < n_e < 10^{6.5}$ cm^{-3}). Another advantage is that these diagnostics give a simultaneous estimate of the intrinsic dust reddening, $E(B-V)$, of the emitting clouds.

Ideally, we want to be able to resolve the individual trans-auroral kinematic components for all our objects. Unfortunately, the spectral resolution and signal-to-noise ratio (S/N) for *WHT*/ISIS are lower than for the *VLT*/Xshooter observations used in Rose et al. (2018). This means that the weaker red [O II] and blue [S II] trans-auroral emission lines for the majority of the objects considered in this paper were not sufficiently strong to allow the separation of narrow and broad/intermediate components. In these cases, a single Gaussian profile was fitted in order to estimate the total emission-line fluxes. Note that the densities derived from the total fluxes are generally lower than those derived from the broad component alone (see figs 8 and 10 in Rose et al. 2018). Because the mass outflow rate and kinetic power depends on the inverse of the density, this

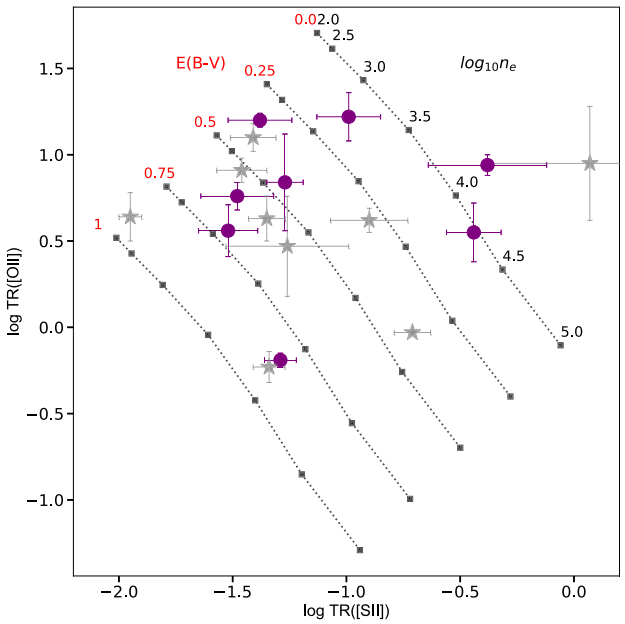

Figure 6. Trans-auroral line ratios for the total emission-line fluxes. The purple circles are the results from this paper. Overplotted as grey stars are the results from Rose et al. (2018).

could lead us to calculate higher values for these outflow properties than Rose et al. (2018).

Fig. 6 shows a plot of log TR([O II]) versus log TR([S II]) for the total emission-line fluxes for the eight objects considered in this paper (purple circles). All fluxes were measured from the *WHT*/ISIS spectra, with the exception of F01004–2237, for which the *HST*/STIS spectrum was used to measure the [S II] λλ4068,4076 flux, and F05189–2524, for which the *HST*/STIS spectrum was used to measure all emission-line fluxes. Also plotted are the measurements from Rose et al. (2018, grey stars).

Overplotted is a grid of ratios predicted by AGN photoionization models, fully described by Rose et al. (2018). The densities based on the total fluxes fall in the range $2.5 < \log n_e\ (\mathrm{cm}^{-3}) < 4.5$, with the median $\log n_e\ (\mathrm{cm}^{-3}) = 3.10 \pm 0.29$. The intrinsic dust reddening falls in the range $0.0 < E(B-V) < 1.0$, with the median $E(B-V) = 0.45 \pm 0.14$. Table 5 gives the density and reddening values obtained using the total emission-line fluxes for each object. These results are consistent with those obtained by Rose et al. (2018) using Xshooter data for the rest of ULIRGs in the QUADROS sample.

For the objects where narrow and intermediate/broad components of the trans-auroral emission lines could be resolved, the associated density and reddening estimates are also shown separately in Tables 6 and 7. Note that F23060+0505 is only included in the Table 6 because only the narrow components of the trans-auroral emission lines were detected. Similarly, F05189–2524 is only included in Table 7 because the whole trans-auroral emission-line profiles are blueshifted with respect to the rest frame, with no rest-frame narrow component detected. Therefore we assume that, in this case, all of the detected flux is associated with the outflow.

These narrow and broad flux ratios are plotted in Fig. 7 (blue and red circles, respectively), along with the measurements from Rose et al. (2018) (blue and red stars, respectively). Some overlap between the narrow and broad components can be seen; however, considering the sample as a whole, the densities of the broad, outflowing components are generally high ($3.5 < \log n_e\ (\mathrm{cm}^{-3}) < 4.5$ and median $\log n_e\ (\mathrm{cm}^{-3}) = 3.8 \pm 0.2$). In comparison, the median density for the narrow components is an order of magnitude lower: $\log n_e\ (\mathrm{cm}^{-3}) = 2.8 \pm 0.3$.

Clearly, assuming a single low density ($\log n_e\ (\mathrm{cm}^{-3}) \sim 2$) for AGN-induced outflows, as is common in many outflow studies, is not justified and is likely to lead to some of the higher values of the mass outflow rates and kinetic powers in the literature.

Despite the previously mentioned degeneracies in the [N II] + Hα fits, as a check we have also determined the intrinsic reddening ($E(B-V)$) based on the Hα/Hβ ratios for the individual components. The estimates are shown in column 6 of Tables 5–7. In general, the two techniques are consistent within 3σ. This is illustrated in Fig. 8 for the total, narrow, and broad fluxes. Interestingly, and consistent with Rose et al. (2018), we find no clear evidence that the outflowing gas is reddened more than the narrow-line gas associated with the host galaxy. Indeed, the narrow-component ratios cover a similar range of reddening as the broad, outflowing components and are, on average, higher. Based on the reddening estimates derived from the Balmer decrements of the ULIRGs considered in this paper, we find median $E(B-V)_{\mathrm{narrow}} = 0.52 \pm 0.09$; and median $E(B-V)_{\mathrm{broad}} = 0.15 \pm 0.25$.

As a reference to compare with the trans-auroral estimates, we also measured the density of the gas emitting the narrow-line components using the [S II] λλ6716/6731 doublet ratio, in which the narrow components are generally strong and well resolved. This technique is not appropriate for the broad components due both to degeneracies in the fit and the fact that in most cases the ratio of the broad components was constrained to the high-density limit during the fitting process. The estimated densities are presented in Table 6, column 5. For the majority of objects the narrow-component ratios were less than 3σ from the low-density limit. For these, we provide a 3σ upper limit on the density.

In all cases, the density estimates and upper limits derived from the [S II] λλ6716/6731 doublet ratios for the narrow components are lower than those derived from the ratios of both the total and broad trans-auroral fluxes, although in the case of F17044+6720 the two estimates are close. These results support the conclusion that the outflows have higher densities than the regions emitting the narrow components.

3.3 Bolometric luminosities

In order to compare the kinetic powers that we derive for the warm outflows with the total radiative powers of the AGN, their bolometric luminosities (L_{bol}) must first be determined. To do this, we used the [O III] λ5007 emission-line luminosity, which has been shown to be a reasonable indicator of the AGN power (Heckman et al. 2004; Dicken et al. 2014). We adopted two approaches for determining L_{bol}: (1) the bolometric correction of Heckman et al. (2004): $L_{\mathrm{bol}} = 3500 L_{[\mathrm{O\,III}]}$, where $L_{[\mathrm{O\,III}]}$ has not been corrected for dust extinction; and (2) the bolometric correction factors of Lamastra et al. (2009) which uses the reddening-corrected $L_{[\mathrm{O\,III}]}$. The correction factors are 87, 142, and 454 for reddening-corrected luminosities of $\log L_{[\mathrm{O\,III}]} =$ 38–40, 40–42, and 42–44 erg s^{-1}, respectively.

For our bolometric luminosity determinations, we used the total [O III] λ5007 fluxes, which involves the assumption that there is little contribution to [O III] λ5007 from stellar photoionized regions. This is a reasonable assumption for our ULIRGs, based on the BPT (Baldwin, Phillips & Terlevich) diagnostic diagrams presented in Rodríguez Zaurín et al. (2013), which suggest that the warm

Table 5. The log n_e and $E(B-V)$ values determined using the *total* trans-auroral emission-line fluxes. Column (5) shows the $E(B-V)$ estimates obtained using the trans-auroral lines ratios. Column (6) shows the $E(B-V)$ estimates obtained using the H α/H β Balmer decrement.

Object name IRAS (1)	log[S II] (2)	log[O II] (3)	log(n_e) (cm^{-3}) (4)	$E(B-V)_{trans}$ (5)	$E(B-V)_{Bal}$ (6)
F01004−2237	-0.38 ± 0.26	0.94 ± 0.06	$4.00^{+0.25}_{-0.30}$	-0.15 ± 0.20	0.04 ± 0.16
F05189−2524	-0.44 ± 0.12	0.55 ± 0.17	$4.25^{+0.25}_{-0.25}$	$0.02^{+0.15}_{-0.15}$	0.29 ± 0.25
F14394+5332E	-1.48 ± 0.16	0.76 ± 0.08	$2.90^{+0.30}_{-0.40}$	$0.60^{+0.15}_{-0.15}$	0.82 ± 0.14
F17044+6720	-1.38 ± 0.14	1.20 ± 0.04	$2.50^{+0.30}_{-0.50}$	$0.35^{+0.10}_{-0.10}$	0.51 ± 0.11
F17179+5444	-1.52 ± 0.13	0.56 ± 0.15	$3.05^{+0.30}_{-0.45}$	$0.70^{+0.15}_{-0.15}$	0.39 ± 0.19
F23060+0505	-1.27 ± 0.08	0.84 ± 0.28	$3.10^{+0.35}_{-0.50}$	$0.45^{+0.15}_{-0.20}$	0.63 ± 0.19
F23233+2817	-0.99 ± 0.14	1.22 ± 0.14	$3.10^{+0.30}_{-0.40}$	$0.15^{+0.15}_{-0.15}$	0.19 ± 0.30
F23389+0303N	-1.29 ± 0.07	-0.19 ± 0.03	$3.95^{+0.10}_{-0.10}$	$0.85^{+0.05}_{-0.05}$	1.24 ± 0.13

Table 6. The log n_e and $E(B-V)$ values determined using the *narrow* emission-line fluxes. Column (4) shows the density estimates obtained using the narrow component of the trans-auroral emission lines, where detected. Column (5) shows the density estimates based on the narrow [S II](6716/6731) flux ratio for comparison. Columns (6) and (7) compare the $E(B-V)$ estimates calculated using the trans-auroral [S II] and [O II] emission blends with those calculated using the H α/H β decrement.

Object name IRAS (1)	log[S II] (2)	log[O II] (3)	log(n_e)$_{trans}$ (cm^{-3}) (4)	log(n_e)$_{(6716/6731)}$ (cm^{-3}) (5)	$E(B-V)_{trans}$ (6)	$E(B-V)_{Bal}$ (7)
F01004−2237	–	–	–	<2.60	–	0.75 ± 0.11
F05189−2524	–	–	–	$2.81^{+0.14}_{-0.14}$		0.47 ± 0.27
F14394+5332E	-1.58 ± 0.25	0.85 ± 0.05	$2.70^{+0.35}_{-0.50}$	<2.64	$0.63^{+0.17}_{-0.18}$	0.91 ± 0.09
F17044+6720	–	–	–	$2.49^{+0.15}_{-0.18}$	–	0.65 ± 0.06
F17179+5444	–	–	–	–	–	–
F23060+0505	-1.27 ± 0.08	0.84 ± 0.28	$3.15^{+0.30}_{-0.50}$	<2.88	$0.45^{+0.15}_{-0.18}$	0.51 ± 0.18
F23233+2817	–	–	–	<2.55	–	0.52 ± 0.16
F23389+0303N	-1.43 ± 0.14	1.06 ± 0.32	$2.60^{+0.60}_{-0.60}$	<2.91	$0.45^{+0.20}_{-0.20}$	0.40 ± 0.09

Table 7. The log n_e and $E(B-V)$ values determined using the *broad* trans-auroral emission-line fluxes. Note that the results for F05189−2524 were obtained using *HST*/STIS data (also in Table 5).

Object name IRAS (1)	log[S II] (2)	log[O II] (3)	log(n_e) (cm^{-3}) (4)	$E(B-V)_{trans}$ (5)	$E(B-V)_{Bal}$ (6)
F01004−2237	–	–	–	–	-0.20 ± 0.20
F05189−2524	-0.44 ± 0.12	0.55 ± 0.17	$4.25^{+0.25}_{-0.25}$	$0.02^{+0.15}_{-0.15}$	0.18 ± 0.24
F14394+5332E	-1.24 ± 0.30	0.37 ± 0.14	$3.55^{+0.45}_{-0.45}$	$0.63^{+0.22}_{-0.30}$	0.70 ± 0.21
F17044+6720	–	–	–	–	-0.35 ± 0.67
F17179+5444	–	–	–	–	0.11 ± 0.37
F23060+0505	–	–	–	–	1.10 ± 0.18
F23233+2817	–	–	–	–	-0.06 ± 0.45
F23389+0303N	-1.27 ± 0.06	-0.51 ± 0.03	$4.20^{+0.10}_{-0.10}$	$0.90^{+0.05}_{-0.05}$	1.48 ± 0.14

gas is dominated by AGN photoionization. Although F05189–2524 was not included in the latter paper, our own BPT analysis shows that the line ratios for this object are also consistent with AGN photoionization.

We determined our luminosities using the measured [O III] λ5007 fluxes. For technique (2), the luminosities were corrected for dust extinction using the total $E(B-V)$ values from column 5 in Table 5 and the extinction law of Calzetti et al. (2000). The calculated luminosities are shown in Table 8, where the estimates obtained using the corrections of Heckman and Lamastra are compared in column 6. The estimates are consistent to within a factor of ∼5 for most of the objects; however, for the three objects with the lowest dust extinction (F01004–2237, F05189–2524, and F23233+2817), the Lamastra estimates are over an order of magnitude lower than the Heckman estimates. We argue that the Heckman correction is likely the most appropriate for these cases due to the small amount of reddening. Therefore, we use only the Heckman-derived bolometric luminosities in the following analyses.

4 MASS OUTFLOW RATES AND POWERS

The key parameters for quantifying the importance of AGN-driven outflows are mass outflow rate and kinetic power. Following the arguments of Rose et al. (2018), we consider the following two cases, based on two different assumptions about the kinematics.

4.1 Using flux-weighted mean outflow velocities, ignoring projection effects

The mass outflow rate ($\dot{M}$) is given by:

$$\dot{M} = \frac{L(H\beta) m_p v_{out}}{\alpha_{eff}^{H\beta} h \nu_{H\beta} n_e R_{out}} \quad (4)$$

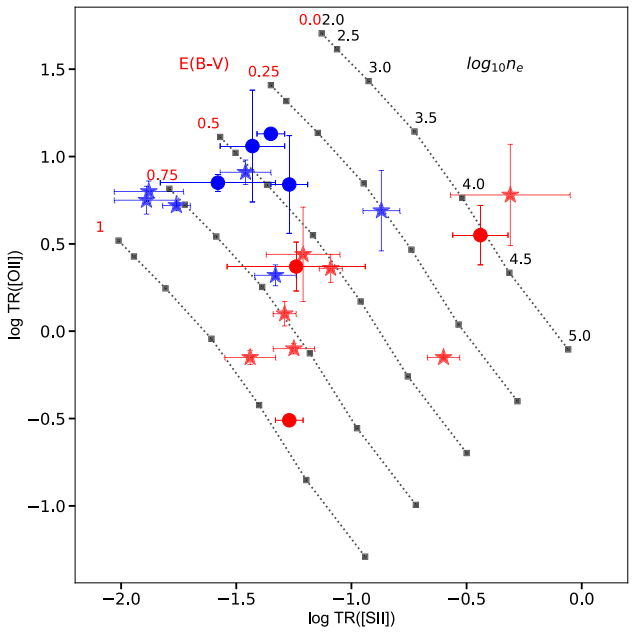

Figure 7. Trans-auroral line ratios for the narrow and broad component fluxes. The solid blue and red circles indicate the narrow and broad components, respectively, for the objects in this paper. Overplotted as blue and red stars are the narrow and broad ratios from Rose et al. (2018).

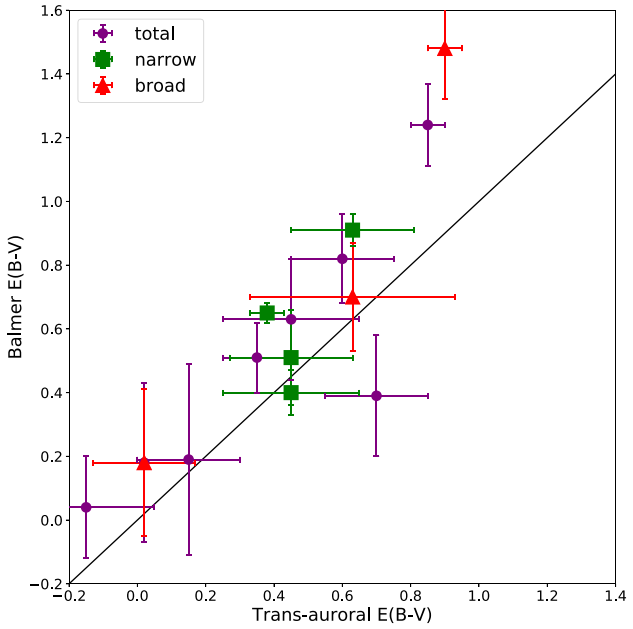

Figure 8. The reddening estimates obtained from the Balmer decrement and trans-auroral line ratios for the emission-line fluxes for the different kinematic components. The black solid line represents a one-to-one ratio. The two techniques are consistent to within 3σ.

where $v_{\rm out}$ is the assumed velocity of the outflowing gas, measured from the Gaussian fits, $R_{\rm out}$ is the outflow radius, $L(\mathrm{H}\,\beta)$ is the intrinsic (i.e. extinction-corrected) H β emission-line luminosity for the outflowing gas (broad + intermediate components), $n_{\rm e}$ is the electron density derived from the trans-auroral emission-line ratios, $m_{\rm p}$ is the proton mass, $\alpha_{\rm eff}^{H\beta}$ is the Case B effective recombination coefficient of H β for $T_{\rm e} = 10^4$K ($\alpha_{\rm eff}^{\rm H\beta} = 3.03 \times 10^{-14}\,\mathrm{cm^3\,s^{-1}}$), taken from Osterbrock & Ferland 2006), and $h\nu_{\rm H\beta}$ is the energy of an H β photon.

In this first scenario, we took the mean velocity shift of the outflowing component of [OIII] with respect to the galaxy rest frame to represent $v_{\rm out}$. For those objects with two or more outflowing components, we calculated a flux-weighted mean. For the radius we used the *HST* estimate where available from Table 4. In the three objects where this is not possible, we used the *WHT*/ISIS estimate, and for F23389+0303N, we have used the radial extent of the double-lobed radio source. To calculate $L(\mathrm{H}\,\beta)$, we used the appropriate $E(B-V)$ derived from the trans-auroral flux ratios.

The outflow power was then calculated using the following equation:

$$\dot{E} = \frac{\dot{M}}{2}(v_{\rm out}^2 + 3\sigma^2) \qquad (5)$$

where σ is the line-of-sight (LoS) velocity dispersion ($\sigma \approx$ FWHM/2.355) calculated using the FWHM of [OIII] for the outflowing gas component. Again, for those objects with more than one outflowing component, we used a flux-weighted mean FWHM. This technique assumes that all of the emission-line broadening is due to turbulence in the gas and that $v_{\rm out}$ represents the true outflow velocity. Note that, in this method, we *did not* correct for the effects of projection on the measured velocities.

We have also expressed the outflow kinetic power as a fraction of the AGN radiative power ($\dot{F}$) by dividing $\dot{E}$ by $L_{\rm bol}$. The calculated values of $v_{\rm out}$, FWHM, $\dot{M}$, $\dot{E}$, and $\dot{F}$ are presented in Table 9. In addition, for the objects where we could only derive upper limits in the outflow radius, the values of the kinetic power, mass outflow rate, and AGN fraction given in Table 9 are lower limits.

Note that, unlike Rose et al. (2018), most of the estimates are based on density values derived from total trans-auroral fluxes (designated 'T' in column 2). This is due to the lower spectral resolution and S/N for *WHT*/ISIS compared with *VLT*/Xshooter. However, in two cases – F14394+5332E and F23389+0303N – we also present estimates based on density values derived from the broad trans-auroral line fluxes alone (designated 'B' in column 2). Moreover, in the case of F05189–2524, the total trans-auroral fluxes are representative of the broad, outflowing components. Overall, we regard the estimates of the outflow properties based on the densities derived from the broad outflowing components in F14394+5332E, F05189–2524, and F23389+0303N as being the most reliable.

In the cases where $\mathrm{R_{[O\,III]}}$ is resolved, we find mass outflow rates in the range $0.06 < \dot{M} < 6\,\mathrm{M_\odot\,yr^{-1}}$ and kinetic powers in the range $1.8 \times 10^{40} < \dot{E} < 4.3 \times 10^{42}\,\mathrm{erg\,s^{-1}}$. These ranges are consistent with those found in Rose et al. (2018), but show little overlap with those calculated by Harrison et al. (2012), Liu et al. (2013), and McElroy et al. (2015) who find larger mass outflow rates and kinetic powers for type-2 AGN using a similar method. Our results are more consistent with those of Harrison et al. (2014), and overlap very well with the results of Villar-Martín et al. (2016).

Comparing the calculated outflow kinetic powers with the bolometric luminosities of the AGN, we find values in the range $4 \times 10^{-3} < \dot{F} < 0.5$ per cent.

4.2 Using maximal outflow velocities to account for projection effects

The estimates made in Section 4.1 are likely to underestimate the true values, due to the fact that use of the mean outflow veloci-

Table 8. [O III] λ5007 luminosities and associated bolometric luminosities. Column (2): uncorrected [O III] luminosity. Column (3): extinction-corrected [O III] luminosity based on the $E(B-V)$ values derived from the total trans-auroral flux ratios and extinction law of Calzetti et al. (2000). Column (4): the [O III] bolometric luminosity based on the Heckman bolometric correction factor. Column (5): the [O III] luminosity based on the appropriate Lamastra bolometric correction factor. Column (6): the ratio of the Heckman bolometric luminosity to the Lamastra bolometric luminosity.

Object name IRAS (1)	$L_{[O\,III]-unc}$ (erg s^{-1}) (2)	$L_{[O\,III]-corr}$ (erg s^{-1}) (3)	$L_{bol-Heck}$ (erg s^{-1}) (4)	$L_{bol-Lam}$ (erg s^{-1}) (5)	Heck/Lam (6)
F01004−2237	(2.5 ± 0.1)E+41	(3.0 ± 1.4)E+41	(8.8 ± 0.4)E+44	(4.2 ± 2.0)E+43	21
F05189−2524	(1.0 ± 0.1)E+41	(1.1 ± 0.5)E+41	(3.6 ± 0.1)E+44	(1.6 ± 0.7)E+43	23
F14394+5332E	(2.6 ± 0.1)E+41	(3.1 ± 1.4)E+42	(9.0 ± 0.2)E+44	(1.4 ± 0.6)E+45	0.64
F17044+6720	(9.9 ± 0.2)E+40	(4.3 ± 1.4)E+41	(3.3 ± 0.1)E+44	(6.1 ± 2.0)E+43	5.7
F17179+5444	(1.7 ± 0.1)E+41	(3.2 ± 1.5)E+42	(6.1 ± 0.1)E+44	(1.5 ± 0.7)E+45	0.41
F23060+0505	(1.3 ± 0.1)E+42	(8.6 ± 3.6)E+42	(4.6 ± 0.4)E+45	(3.9 ± 1.6)E+45	1.2
F23233+2817	(4.8 ± 0.2)E+41	(8.9 ± 4.0)E+41	(1.7 ± 0.1)E+45	(1.3 ± 0.6)E+44	13
F23389+0303N	(6.7 ± 0.1)E+41	(2.3 ± 0.4)E+43	(2.4 ± 0.1)E+45	(1.1 ± 0.2)E+46	0.22

Table 9. Outflow properties for the flux-weighted mean velocity case. Column (2): the trans-auroral fluxes used to calculate the density and reddening values employed in the calculations: T = total and B = broad/intermediate. In the case of F05189–2524, the whole profile is blueshifted with respect to the rest frame and hence the total and broad fluxes are assumed to be equivalent. Column (3): the flux-weighted mean velocity. Column (4): the flux-weighted mean FWHM. Column (5): the calculated mass outflow rate. Column (6): the calculated kinetic power. Column (7): the kinetic power expressed as a fraction of the bolometric luminosity ($\dot{E}/L_{bol}$).

Object name IRAS (1)	Component T/B (2)	v_{mean} (km s^{-1}) (3)	FWHM (km s^{-1}) (4)	$\dot{M}$ (M$_\odot$ yr^{-1}) (5)	$\dot{E}$ (erg s^{-1}) (6)	$\dot{F}$ (per cent) (7)
F01004−2237	T	− 826 ± 52	1302 ± 35	$0.5^{+1.0}_{-0.3}$	$(2.5^{+6.2}_{-1.9}) \times 10^{41}$	$(2.8^{+7.5}_{-2.1}) \times 10^{-2}$
F05189−2524	T,B	− 688 ± 31	949 ± 32	$0.06^{+0.10}_{-0.04}$	$(1.8^{+3.4}_{-1.3}) \times 10^{40}$	$(5.1^{+9.8}_{-3.6}) \times 10^{-3}$
F14394+5332E	T	− 990 ± 89	1616 ± 27	$5.5^{+16.9}_{-4.1}$	$(4.2^{+14.4}_{-3.2}) \times 10^{42}$	$0.47^{+1.65}_{-0.36}$
	B	″	″	$1.4^{+6.2}_{-1.3}$	$(1.1^{+5.3}_{-1.0}) \times 10^{42}$	$0.12^{+0.60}_{-0.11}$
F17044+6720	T	− 503 ± 85	1754 ± 60	$0.3^{+1.2}_{-0.2}$	$(1.8^{+8.1}_{-1.3}) \times 10^{41}$	$(5.2^{+24.0}_{-3.7}) \times 10^{-2}$
F17179+5444	T	− 241 ± 78	1528 ± 32	$3.2^{+26.0}_{-2.6}$	$(1.3^{+11.8}_{-1.1}) \times 10^{42}$	$0.22^{+1.96}_{-0.18}$
F23060+0505	T	− 461 ± 63	1023 ± 48	$0.8^{+3.2}_{-0.6}$	$(1.9^{+9.5}_{-1.5}) \times 10^{41}$	$(4.0^{+22.8}_{-3.4}) \times 10^{-3}$
F23233+2817	T	− 391 ± 35	940 ± 17	>0.04	$>6.6 \times 10^{39}$	$>4.0 \times 10^{-4}$
F23389+0303N[a]	T	− 134 ± 36	2345 ± 37	>0.2	$>1.4 \times 10^{41}$	$>6.0 \times 10^{-3}$
	B	″	″	>0.1	$>1.30 \times 10^{41}$	$>5.4 \times 10^{-4}$
F23389+0303N[b]	T	− 134 ± 36	2345 ± 37	$0.9^{+3.8}_{-0.6}$	$(8.9^{+37.7}_{-5.6}) \times 10^{41}$	$(3.8^{+16.4}_{-2.4}) \times 10^{-2}$
	B	″	″	$0.7^{+2.7}_{-0.4}$	$(6.2^{+26.3}_{-3.9}) \times 10^{41}$	$(2.6^{+11.4}_{-1.7}) \times 10^{-2}$

Notes. [a]These estimates were made using the upper limit on the outflow radius from the *WHT*/ISIS spectrum.
[b]These estimates were made using the radius estimate of the radio lobes ($R = 415$ pc) as a proxy for the outflow radius, taken from Nagar et al. (2003). This assumes that the outflows are jet-driven.

ties of the outflowing components does not take into account LoS projection effects, as discussed in Rose et al. (2018).

A more physical approach is to assume that the broadening of the emission lines is due entirely to different projections of the velocity vector of the expanding outflow with respect to the LoS, rather than due to turbulence. Therefore, the true velocity of the outflowing gas is given by the extreme blue wing of the Gaussian profile. This corresponds to the gas travelling directly towards us along the LoS. It follows that, in this scenario, the outflow kinetic power is given by dropping the turbulence term in equation (5), and taking the v_{05} shift of the Gaussian fit to the outflow component relative to the galaxy rest frame to represent v_{out}, rather than the mean shift as before. Note we used v_{05} rather than v_{00} to avoid confusion with the continuum. The estimates derived using this method are presented in Table 10.

Under the maximal velocity assumption, and considering the estimates for the objects in which $R_{[O\,III]}$ is resolved, we find mass outflow rates in the range $0.1 < \dot{M} < 20\,M_\odot\,yr^{-1}$ and kinetic powers in the range $9.3 \times 10^{40} < \dot{E} < 2.3 \times 10^{43}$ erg s^{-1}. These ranges are again consistent with those found in Rose et al. (2018), and the kinetic powers are a factor of ∼5× higher than those obtained using the first method.

Comparing the outflow kinetic powers with the bolometric luminosities of the AGN, we find values in the range $0.02 < \dot{F} < 3$ per cent. While the fraction of the AGN power contained in the outflow is naturally larger when using higher velocities, even in this maximal velocity case, the kinetic power and mass outflow rates still show little overlap with the results of Harrison et al. (2012), Liu et al. (2013), and McElroy et al. (2015) and fall short of the threshold required ($\dot{F} = 5$–10 per cent) by the Di Matteo et al. (2005) and Springel et al. (2005) models.

Initially, these results may suggest that the AGN-induced outflows alone do not contain the necessary energy to significantly impact their host galaxies. However, we note that some caution is required when comparing our $\dot{F}$ results with the predictions of theoretical models for AGN-induced outflows. As discussed in Har-

Table 10. Outflow properties for the maximal velocity case using the v_{05} velocities. Column (2): thetrans-auroral fluxes used to calculate the density and reddening values employed in the calculations: T = total and B = broad/intermediate. In the case of F05189–2524, the whole profile is blueshifted with respect to the rest frame and hence the total and broad fluxes are assumed to be equivalent. Column (3): the v_{05} velocity. Column (4): the calculated mass outflow rate. Column (5): the calculated kinetic power. Column (6): the fraction of AGN bolometric luminosity contained within the outflow ($\dot{E}/L_{\rm bol}$).

Object name IRAS (1)	Component T/B (2)	v_{05} (km s^{-1}) (3)	$\dot{M}$ (M$_\odot$ yr^{-1}) (4)	$\dot{E}$ (erg s^{-1}) (5)	$\dot{F}$ (per cent) (6)
F01004−2237	T	-1932 ± 82	$1.0^{+2.2}_{-0.7}$	$(1.2^{+2.9}_{-0.9}) \times 10^{42}$	$0.14^{+0.35}_{-0.10}$
F05189−2524	T,B	-1494 ± 58	$0.13^{+0.21}_{-0.09}$	$(9.3^{+17.0}_{-6.5}) \times 10^{40}$	$(2.6^{+4.9}_{-1.8}) \times 10^{-2}$
F14394+5332E	T	-2362 ± 112	$13.2^{+37.4}_{-9.7}$	$(2.3^{+7.5}_{-1.8}) \times 10^{43}$	$2.6^{+8.6}_{-2.0}$
	B	$''$	$3.4^{+13.8}_{-3.0}$	$(6.0^{+27.4}_{-5.4}) \times 10^{42}$	$0.66^{+3.12}_{-0.60}$
F17044+6720	T	-1992 ± 136	$1.2^{+3.8}_{-0.8}$	$(1.5^{+5.7}_{-1.0}) \times 10^{42}$	$0.42^{+1.69}_{-0.30}$
F17179+5444	T	-1539 ± 105	$20.1^{+72.9}_{-14.9}$	$(1.5^{+6.5}_{-1.2}) \times 10^{43}$	$2.5^{+10.7}_{-1.9}$
F23060+0505	T	-1330 ± 104	$2.2^{+8.1}_{-1.7}$	$(1.2^{+5.5}_{-1.0}) \times 10^{42}$	$(2.7^{+13.2}_{-2.2}) \times 10^{-2}$
F23233+2817	T	-1189 ± 49	>0.11	$>4.7 \times 10^{40}$	$>9.5 \times 10^{-2}$
F23389+0303N[a]	T	-2126 ± 67	>3.3	$>4.4 \times 10^{42}$	>0.18
	B	$''$	>2.3	$>3.2 \times 10^{42}$	>0.13
F23389+0303N[b]	T	-2126 ± 67	$14.9^{+16.0}_{-7.3}$	$(2.1^{+2.6}_{-1.1}) \times 10^{43}$	$0.91^{+1.13}_{-0.48}$
	B	$''$	$10.4^{+11.1}_{-5.1}$	$(1.5^{+1.8}_{-0.8}) \times 10^{43}$	$0.63^{+0.79}_{-0.33}$

Notes. [a]These estimates were made using the upper limit on the outflow radius from the *WHT*/ISIS spectrum.
[b]These estimates were made using the radius estimate of the radio lobes ($R = 415$ pc) as a proxy for the outflow radius, taken from Nagar et al. (2003). This assumes that the outflows are jet-driven.

rison et al. (2018), it may not be appropriate to directly compare the $\dot{E}/L_{\rm bol}$ values required by the models with the $\dot{F}$ values we estimate for the warm outflows in ULIRGs: first, the $\dot{E}$ used in some of the models (e.g. Di Matteo et al. 2005; Springel et al. 2005) represents the thermal energy deposited in the near-nuclear gas by the AGN, rather than the kinetic power in the outflow; and second, not all of the kinetic power associated with an inner (e.g. accretion disc) wind generated by an AGN may be transmitted to the cooler, larger scale outflow that we observe in the optical emission lines, due to radiative cooling, and work against gravity and external pressure as the outflow expands. Indeed, some recent theoretical studies suggest that as little as 10 per cent of the nuclear wind power (or ∼0.5 per cent $L_{\rm bol}$) is transmitted to the large-scale outflow (Richings & Faucher-Giguère 2018). This is consistent with the direct observational comparisons that have been made between the kinetic powers of the inner high-ionization wind and outer molecular outflow in the case of the ULIRG F11119+3257 (Tombesi et al. 2015; Veilleux et al. 2017). Such a low coupling efficiency is also consistent with the multistage outflow model of Hopkins & Elvis (2010). Therefore, our estimates of the coupling efficiency for the warm ionized gas ($0.02 < \dot{F} < 3$ per cent) are in line with some of the most recent theoretical predictions.

4.3 Comparison with neutral and molecular outflows

Estimates for the mass outflow rates and kinetic powers for the neutral and molecular outflow phases for five of the ULIRGs in the full QUADROS sample are available in the literature. These values are shown in Table 11.

Rupke et al. (2005) estimated the properties of the neutral outflows in F05189–2524, F13451–1232, and F23389+0303N based on the Na ID absorption line. An additional estimate for the neutral mass outflow rate of F13451–1232, determined using the HI 21 cm line, is provided by Morganti et al. (2013). The neutral and ionized mass outflow rates are comparable in the case of F13451–1232, however the estimated neutral mass outflow rates are significantly higher for the other two objects. The kinetic power of the neutral outflow, on the other hand, is two orders of magnitude greater than that of the ionized outflow in the case of F05189–2524, significantly lower in the case of F13451–1232, and comparable in the case of F23389+0303N.

Estimates for the molecular mass outflow rates in F05189–2524, F14378–3651, and F23060+0505 are provided by González-Alfonso et al. (2017) and Cicone et al. (2014). In all cases, the molecular mass outflow rates are significantly greater than those of the ionized outflows. González-Alfonso et al. (2017) also provide estimates for the kinetic powers of the molecular outflow for F05189–2524 and F14378–3651. In the former case, the molecular kinetic power is significantly larger than that of the ionized outflow, and comparable with the kinetic power of the neutral outflow. In the latter case, the kinetic power measured for the molecular outflow is two orders of magnitude higher than the lower limit derived for the ionized outflow.

The larger mass outflow rates and kinetic powers for the cooler gas components are consistent with the idea that the gas has been accelerated in fast shocks, with the neutral and molecular gas then accumulating as the warm gas cools behind the shock fronts (Tadhunter et al. 2014; Zubovas & King 2014; Morganti 2015; Richings & Faucher-Giguère 2018).

5 LINKS BETWEEN THE WARM OUTFLOW PROPERTIES AND AGN PROPERTIES

Some observational studies have found evidence for correlations between the properties of the outflows and those of the AGN. For example, Fiore et al. (2017) find evidence for strong correlations between the mass outflow rates and the AGN bolometric luminosities of both molecular and ionized outflows. Similarly, Cicone et al. (2014) show evidence for a correlation between $L_{\rm bol}$ and the kinetic powers of molecular outflows. Given the assumption that our

Table 11. A comparison between the ionized, neutral, and molecular outflow phases, where estimates are available for the QUADROS sample. The subscripts are as follows: I = ionized; N = neutral; and M = molecular. The estimates for the ionized outflows (maximal velocity case) are taken from this paper and Rose et al. (2018). The references for the neutral and molecular outflow measurements are denoted by the superscript letters.

Object name IRAS (1)	$\dot{M}_{\rm I}$ ($M_\odot yr^{-1}$) (2)	$\dot{M}_{\rm N}$ ($M_\odot yr^{-1}$) (3)	$\dot{M}_{\rm M}$ ($M_\odot yr^{-1}$) (4)	$\log(\dot{E}_{\rm I})$ (erg s^{-1}) (5)	$\log(\dot{E}_{\rm N})$ (erg s^{-1}) (6)	$\log(\dot{E}_{\rm M})$ (erg s^{-1}) (7)
F05189−2524	$0.13^{+0.21}_{-0.09}$	117^{a}	270^{+22}_{-130} [b]	$40.97^{+0.45}_{-0.52}$	43.08^{a}	$43.2^{+0.1}_{-0.2}$ [b]
F13451−1232W	$10.5^{+2.8}_{-2.3}$	7.6^{a}	–	43.34 ± 0.11	41.67^{a}	–
		$16–29^{c}$				
F14378−3651	>0.082	–	180^{+180}_{-33} [b]	>40.76	–	43.1 ± 0.2 [b]
F23060+0505	$2.2^{+8.1}_{-1.7}$	–	1500^{d}	$42.08^{+0.74}_{-0.78}$	–	–
F23389+0303N	$10.4^{+11.1}_{-5.1}$	$>49^{a}$	–	43.2 ± 0.3	$>42.4^{a}$	–

Notes. [a]Rupke et al. (2005).
[b]González-Alfonso et al. (2017).
[c]Morganti et al. (2013).
[d]Cicone et al. (2014).

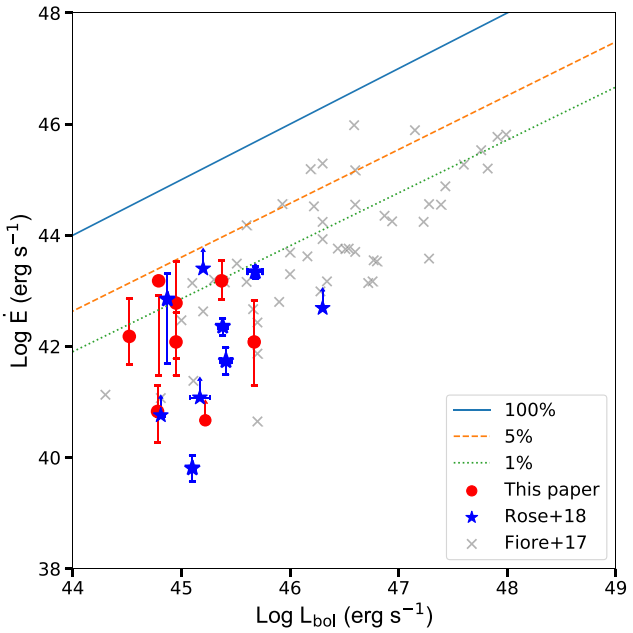

Figure 9. Outflow kinetic power versus AGN bolometric luminosity for the maximal v_{05} velocity case. The bolometric luminosities were determined using the total emission-line flux of [OIII] λ5007. The kinetic powers of the outflow were determined using the broad, blueshifted components of the H β emission line, and the best available density estimates (i.e. using the broad trans-auroral fluxes where possible). The red circles and blue stars represent the results from this paper and Rose et al. (2018), respectively. The overplotted lines represent $\dot{F} = 100$ per cent (solid), 5 per cent (dashed), and 1 per cent (dotted). Also overplotted for comparison are the results of Fiore et al. (2017) for 51 AGN (grey crosses). Note that caution must be taken when directly comparing the QUADROS and Fiore et al. (2017) results due to the different methodologies employed for calculation of the outflow parameters.

ionized outflows are AGN-driven (see Section 3.3), we have also examined this within our data.

In Fig. 9, we plot the outflow kinetic power ($\dot{E}$) for the maximal v_{05} velocity case against the bolometric luminosity of the AGN for the full QUADROS sample. The red circles represent the results from this paper and the blue stars represent the results of Rose et al. (2018). We have used the best available estimate of the kinetic power for each object[3] and have taken the most appropriate bolometric luminosity correction as discussed in Section 3.3 in this paper, and section 3.3 in Rose et al. (2018).

Overplotted are three lines corresponding to the fraction of the AGN luminosity contained in the kinetic power of the outflow ($\dot{F}$): 100 per cent (solid), 5 per cent (dashed), and 1 per cent (dotted). Although the majority of the sample fall well below the 1 per cent line, a significant proportion (∼35 per cent) of the QUADROS ULIRGs fall close to, or above it. For reference, we also overplot the results of Fiore et al. (2017) for 51 AGN, for which they claim a significant correlation between $L_{\rm bol}$ and $\dot{E}$. Considering only the QUADROS results, for which we have attempted to constrain the outflow parameters in a precise and consistent manner, we find no significant correlation between the kinetic powers of the outflows and the AGN bolometric luminosities – a p-value of 0.47 means we cannot reject the null hypothesis that the two sets of data are uncorrelated.[4] However, this apparent difference from the results of Fiore et al. (2017) is perhaps not surprising, given the small range of AGN luminosity covered by our sample and the relatively high degree of scatter.

We have also considered potential correlations between the AGN bolometric luminosities and other outflow properties such as the outflow velocities, radii, and mass outflow rates, as plotted in Fig. 10. In all three plots, the red circles, blue stars, and grey crosses represent the results from this paper, Rose et al. (2018), and Fiore et al. (2017), respectively. We find no statistically significant correlation between $L_{\rm bol}$ and outflow velocity within the QUADROS sample ($p = 0.49$). Furthermore, we find little evidence for a significant correlation between $L_{\rm bol}$ and either $\dot{M}$ ($p = 0.11$) or radius ($p = 0.76$). Again, this lack of correlation could perhaps be explained by the high scatter and narrow luminosity range.

Interestingly, the QUADROS results fall within the scatter of the lower end of the $\dot{E}$ and $\dot{M}$ correlations of Fiore et al. (2017) shown in Figs 9 and 10(c). However, this apparent agreement may

[3]For this and the subsequent plots, we have used the estimates of the outflow properties derived from the broad component fluxes of the trans-auroral emission lines, where available. For the objects where the individual kinematic components were unresolved, we have used the estimates derived from the total emission-line fluxes.
[4]When calculating the Spearman rank-order correlation statistics, we have included the upper/lower limits as if they were measured values.

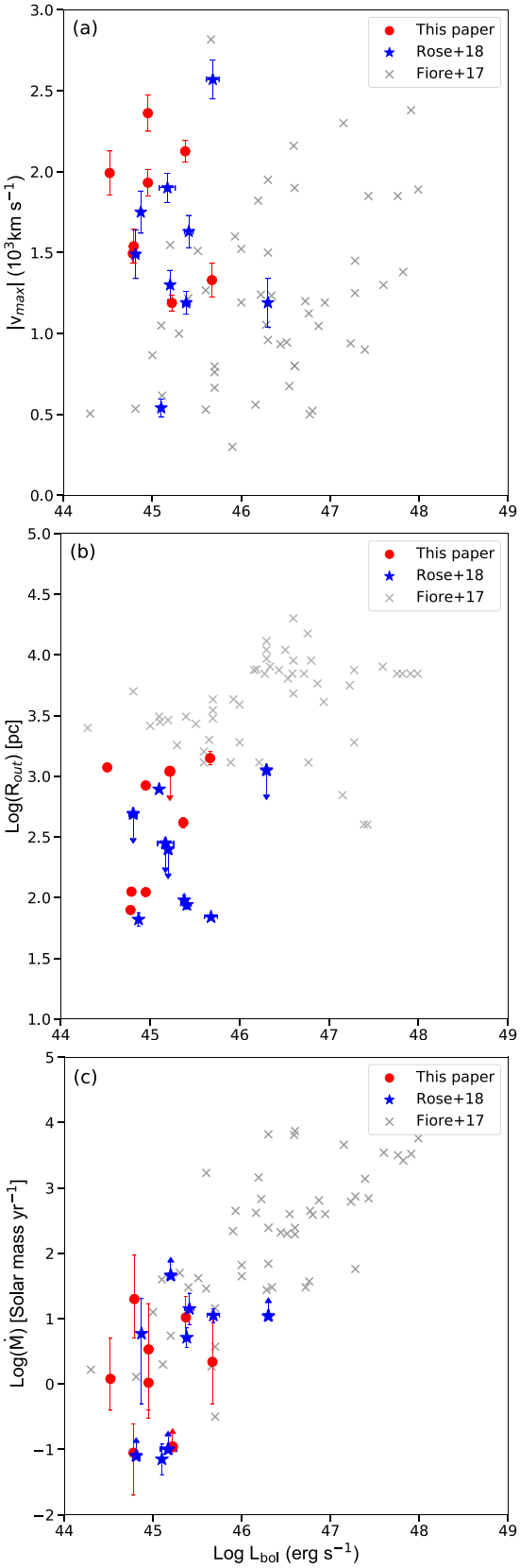

Figure 10. Plots of the outflow properties against log($L_{\rm bol}$) for the full QUADROS sample: (a) v_{05} vs log($L_{\rm bol}$); (b) log($R_{\rm out}$) vs log($L_{\rm bol}$); and (c) log($\dot{M}$) vs log($L_{\rm bol}$). The points are as in Fig. 9.

be misleading: the lower outflow velocities[5] (see Fig. 10a) and larger outflow radii (see Fig. 10b) found by Fiore et al. (2017) may compensate for the lower gas densities (and hence larger total gas masses) assumed in their study.

We note that a lack of correlation between the AGN luminosities and outflow properties is perhaps to be expected. Zubovas (2018) argues that because AGN duty cycles are shorter than the dynamical times of the outflows, any observed outflows greater than around 0.1 kpc in extent are unlikely to have been originally driven by the current phase of AGN activity. Therefore, there is no reason to expect that the currently observed AGN luminosities should correlate with the observed outflow properties, and a high degree of intrinsic scatter is to be expected. Our results appear to be consistent with this conclusion.

6 ORIGIN OF THE TRANS-AURORAL EMISSION LINES

An argument against the use of the trans-auroral lines to measure the densities of the outflows is that the higher critical density species ([S II] λλ4068,4076 and [O II] λλ7319,7331) may originate from dense clouds within a lower density outflow, whereas the lower critical density species could instead originate from the low-density gas (Sun, Greene & Zakamska 2017). If this lower density component contained much of the mass of the outflow, but contributed little to the flux, then this could lead to the trans-auroral diagnostics severely underestimating the mass outflow rates and kinetic powers.

However, as we argue in Rose et al. (2018), any high-density clumps would still be expected to radiate strongly in H β – used to estimate the gas mass – and the electron densities we measure from the trans-auroral line ratios remain below the critical density, $n_{\rm crit}$, of the [O III] λ5007 line ($n_{\rm crit} = 7 \times 10^5$ cm^{-3}), which we use to determine the outflow kinematics and radii. Therefore, depending on the ionization level, we might also expect the high-density clumps to radiate significant [OIII] λ5007 emission.

To investigate this, we have calculated the theoretical ratios of the high-critical-density trans-auroral [OII] and [S II] blends to the [O III] λ5007 and H β lines from a single, radiation bounded, solar abundance cloud, and compared these ratios to those we observe. For these models, we used version C17.00 of CLOUDY, last described by Ferland et al. (2013).

Fig. 11 plots log([O II] λλ7319,7331/[O III] λ5007) against log([S II] λλ4068,4076)/H β). On this plot, we present the results from this paper (red circles) along with those of Rose et al. (2018, blue triangles). Overplotted as dotted and dashed lines are the CLOUDY theoretical grids for densities of 10^3 and 10^4 cm^{-3}, respectively. The grids vary in ionization parameter, log(U), and ionizing power-law spectral index, α, over the respective ranges: $-4 < \log(U) < -1$ and $-2 < \alpha < -1$.

Our observed ratios show good consistency with those predicted by the AGN photoionization models. While the displacement between the two sets of models is not particularly large, we find that the positions of the ULIRGs on the respective grids are consistent with the densities we derive from the trans-auroral line ratio analysis. In particular, all ULIRGs considered in this paper (red circles) fall in the range of densities expected from the trans-auroral emission-line estimates: $10^3 < n_{\rm e} < 10^4$ cm^{-3}.

[5]Note that, instead of v_{05}, Fiore et al. (2017) used the velocity of the peak of the broad component minus 2σ as the outflow velocity.

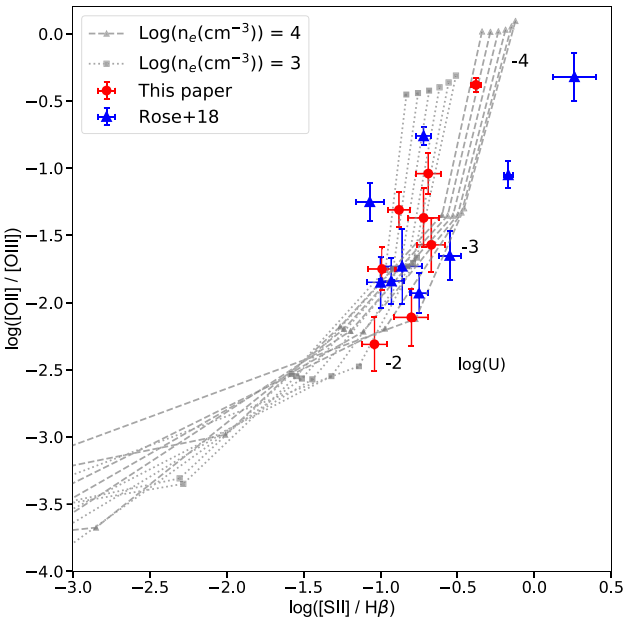

Figure 11. Theoretical photoionization grids modelled with CLOUDY for the total emission-line flux ratios of log([O II] λλ7319,7331/[O III] λ5007) against log([S II] λλ4068,4076)/H β). The dotted lines correspond to a density of 10^3 cm^{-3}. The dashed lines correspond to a density of 10^4 cm^{-3}. The separate lines within these bands correspond to different values of the ionizing power-law spectral index in the range $-2 < \alpha < -1$, and the ionization parameter, log(U), is indicated by the numbers. Overplotted are the ratios we measure from this paper (red circles) and Rose et al. (2018,blue triangles), respectively.

The 66 per cent of the ULIRGs from Rose et al. (2018, blue triangles) also fall in this range; however, in this case the scatter is larger, with three points falling off the grids. The anomalous point to the top right of the grid corresponds to F15462–0450. This object is an unreddened type 1 AGN, and the wing of the broad Hδ emission from this AGN overlaps the blue trans-auroral [S II] λ4073 blend, potentially leading to a higher degree of uncertainty in the flux of this blend and the line ratios derived from it. A further object (F13451+1232W) falls to the right of the log n_e (cm^{-3}) = 4 grid, indicating higher densities. However, this is consistent with the fact that this object shows the highest estimated density of the whole QUADROS sample log n_e (cm^{-3}) = 4.5 ± 0.2). Finally, one object (F14378–3651) falls to the left of the log n_e (cm^{-3}) = 3 grid, consistent with the relatively low density estimated for this object based on the total trans-auroral emission-line fluxes in Rose et al. (2018): log n_e (cm^{-3}) ∼ 2.

Furthermore, as a consistency check, we have directly estimated the ionization parameter, U, defined as the ratio of ionizing photon flux to the gas density, for each ULIRG using the following equation:

$$U = \frac{L_{\rm ion}}{c4\pi R_{\rm out}^2 n_e h\nu_{\rm ion}} \quad (6)$$

where c is the speed of light, $R_{\rm out}$ is the radius of the outflow, n_e is the electron density of the gas, $\nu_{\rm ion}$ is the average ionizing photon frequency ($\nu_{\rm ion} = 1.02 \times 10^{16}$ Hz, Robinson et al. 2000), and $L_{\rm ion}$ is the AGN ionizing continuum luminosity. For these estimations, we assumed $L_{\rm ion} = 0.56 L_{\rm bol}$, based on the results of Netzer & Trakhtenbrot (2014) for AGN with non-rotating, 10^7 M$_\odot$ BHs. Using equation (6), we find that the ULIRGs cover a range in ionization parameter of $-1.3 < \log(U) < -3.4$. Given our assumptions, this is consistent with the range of log(U) covered by the ULIRG ratios on Fig. 11. Therefore, these results provide strong evidence for the idea that the bulk of the flux of all of our diagnostic emission lines originates from the same dense gas structures.

However, it is not possible to rule out the idea that there exists a lower density, higher filling factor gas component in the outflow that has a higher gas mass but makes a relatively minor contribution to the emission-line fluxes. To see this, we consider the case in which a fixed volume V in the outflow contains two gas components with different densities: a higher density component with electron density n_h, volume filling factor f_h, and electron temperature T_h; and a lower density component with electron density n_l, volume filling factor f_l, and electron temperature T_l. For simplicity, we assume that the both components comprise of fully ionized pure hydrogen gas. The H β luminosities of the two components are then given by:

$$L(H\beta)_l = n_l^2 \alpha_{\rm eff}^{H\beta}(T_l) V f_l h\nu_{H\beta} \quad (7)$$

and

$$L(H\beta)_h = n_h^2 \alpha_{\rm eff}^{H\beta}(T_h) V f_h h\nu_{H\beta} \quad (8)$$

and their total gas masses by

$$M_l = m_p n_l V f_l \quad (9)$$

and

$$M_h = m_p n_h V f_h. \quad (10)$$

Combining these equations, and assuming that $\alpha_{\rm eff}^{H\beta}(T_l) = \alpha_{\rm eff}^{H\beta}(T_h)$,[6] we find the following expression for the ratio of the volume filling factors:

$$\left(\frac{f_h}{f_l}\right) = \left(\frac{L(H\beta)_l}{L(H\beta)_h}\right)\left(\frac{M_h}{M_l}\right)^2 \quad (11)$$

and the ratio of the electron densities is given by:

$$\left(\frac{n_h}{n_l}\right) = \left(\frac{f_l}{f_h}\right)\left(\frac{M_h}{M_l}\right). \quad (12)$$

Therefore, it is possible for the low-density component to be 10× more massive than the high-density component ($(M_h/M_l) = 0.1$), yet contribute 10 per cent or less of the H β luminosity of the high-density component (i.e. $L(H\beta)_l/L(H\beta)_h \leq 0.1$), provided that the filling factor and density contrasts satisfy $(f_h/f_l) \leq 10^{-3}$ and $(n_h/n_l) \geq 10^2$, respectively. Given that we find typical volume filling factors for the warm outflows in our ULIRG sample in the range $10^{-6} < f_h < 10^{-3}$, such a high filling factor contrast is feasible. However, it is not clear why warm gas components with densities, and hence pressures, differing by a factor ∼100 should co-exist in the same volume, especially if all the gas has cooled isobarically behind a shock front.

7 CONCLUSIONS

The results of this study of warm outflows in eight nearby ULIRGs with *WHT*/ISIS (QUADROS III) strongly reinforce those obtained for nine ULIRGs using *VLT*/Xshooter by Rose et al. (2018, QUADROS I). After considering the effects of seeing, we find evidence that the ionized outflow regions are compact ($0.08 < R_{\rm out}$

[6]Even in the extreme case that the low-density gas is matter bounded, but the high-density gas is radiation bounded, the temperatures of the two components, and hence the recombination coefficients (Osterbrock & Ferland 2006), are unlikely to differ by more than a factor of ∼2.

< 1.5 kp, median $R_{\rm out} \sim 0.8$ kpc). In addition, we find that the outflows can suffer a significant degree of reddening ($0 < E(B-V) < 1$, median $E(B-V) \sim 0.5$), and have high densities ($2.5 <$ log $n_{\rm e}$ (cm^{-3}) < 4.5, median log $n_{\rm e}$ (cm^{-3}) ~ 3.1).

The resultant mass outflow rates ($0.1 < \dot{M} < 20$ M$_\odot$ yr^{-1}, median $\dot{M} \sim 2$ M$_\odot$ yr^{-1}) and kinetic powers expressed relative to AGN bolometric luminosity ($0.02 < \dot{F} < 3$ per cent, median $\dot{F} \sim 0.3$ per cent) are relatively modest. These values are consistent with the theoretical expectations if it is assumed that the inner winds transmit only a modest fraction (∼10 per cent) of their energy to the large-scale outflows.

We have also used photoionization modelling to show that the bulk of the fluxes of the strong diagnostic emission lines (e.g. H β and [OIII] λλ4959,5007) detected in our spectra are plausibly emitted by the same high-density clouds that emit the trans-auroral [SII] and [O II] density diagnostic lines. However, we cannot entirely rule out the idea that there exists a lower density, higher filling factor warm outflow component that contributes relatively little to the emission-line fluxes, but is substantially more massive.

Considering the QUADROS sample as a whole, we do not find evidence that the properties of the outflows are strongly correlated with the AGN bolometric luminosities. This lack of correlation may be due in part to the relatively narrow range in $L_{\rm bol}$ covered by our sample, coupled with the uncertainties on the $L_{\rm bol}$ values themselves. However, given that we have been careful to accurately measure the key properties of the outflows (radii, densities, and reddenings), it is plausible that there is a high degree of intrinsic scatter (∼2–3 orders of magnitude) in $\dot{M}$, $\dot{E}$, and $\dot{F}$ for a given $L_{\rm bol}$. This scatter could be due to different efficiencies in the coupling between the inner winds and the larger scale interstellar medium (ISM), perhaps related to different circumnuclear environments. Alternatively, it might reflect high-amplitude variability in the AGN radiative outputs.

Indeed, in the case of F01004−2237, we have direct evidence for just such variability: this object has a high-ionization narrow-line spectrum characteristic of AGN, yet lacks a type 1 AGN BLR component, despite the fact that the recent detection of a TDE event in its nucleus demonstrates that our LoS to its central supermassive BH is relatively unobscured (Tadhunter et al. 2017).

Ultimately, the results of the QUADROS project emphasize the importance of determining accurate radii, electron densities, and reddening values for AGN-driven outflows. The dearth of accurate measurements of these parameters is likely to have been at least partially responsible for the lack of consistency between the results and conclusions of the various studies of AGN outflows in the past. Therefore, to gain a complete multiphase understanding of the importance of AGN-driven outflows to galaxy evolution, further high-resolution observations designed specifically to measure radii, reddening, and densities of outflow regions are required.

ACKNOWLEDGEMENTS

MR and CT acknowledge support from STFC. RAWS thanks J. Pierce, H. Stevance, and K. Tehrani for helpful discussions. We also thank the anonymous referee for useful comments and suggestions that enabled us to improve this work. Based on observations obtained with ISIS on the *WHT*, operated on the island of La Palma by the Isaac Newton Group in the Spanish Observatorio del Roque de los Muchachos of the Instituto de Astrofisica de Canarias, and observations taken with STIS on the NASA/ESA *HST*. The authors acknowledge the data analysis facilities provided by the STARLINK Project, which was run by CCLRC on behalf of PPARC. This research has made use of the NASA/IPAC Extragalactic Database which is operated by the Jet Propulsion Laboratory, California Institute of Technology, under contract with NASA.

REFERENCES

Arribas S., Colina L., Bellocchi E., Maiolino R., Villar-Martín M., 2014, A&A, 568, A14
Batcheldor D., Tadhunter C., Holt J., Morganti R., O'Dea C. P., Axon D. J., Koekemoer A., 2007, ApJ, 661, 70
Bruzual G., Charlot S., 2003, MNRAS, 344, 1000
Calzetti D., Armus L., Bohlin R. C., Kinney A. L., Koornneef J., Storchi-Bergmann T., 2000, ApJ, 533, 682
Cano-Díaz M., Maiolino R., Marconi A., Netzer H., Shemmer O., Cresci G., 2012, A&A, 537, L8
Cardelli J. A., Clayton G. C., Mathis J. S., 1989, ApJ, 345, 245
Carniani S. et al., 2015, A&A, 580, A102
Carniani S. et al., 2016, A&A, 591, A28
Cicone C. et al., 2014, A&A, 562, A21
Cid Fernandes R., Mateus A., Sodré L., Stasińska G., Gomes J. M., 2005, MNRAS, 358, 363
Di Matteo T., Springel V., Hernquist L., 2005, Nature, 433, 604
Dicken D. et al., 2014, ApJ, 788, 98
Farrah D., Surace J. A., Veilleux S., Sanders D. B., Vacca W. D., 2005, ApJ, 626, 70
Ferland G. J. et al., 2013, Rev. Mex. Astron. Astrofis., 49, 137
Fiore F. et al., 2017, A&A, 601, A143
González-Alfonso E. et al., 2017, ApJ, 836, 11
Harrison C. M. et al., 2012, MNRAS, 426, 1073
Harrison C. M., Alexander D. M., Mullaney J. R., Swinbank A. M., 2014, MNRAS, 441, 3306
Harrison C. M., Costa T., Tadhunter C. N., Flütsch A., Kakkad D., Perna M., Vietri G., 2018, Nat. Astron., 2, 198
Heckman T. M., Kauffmann G., Brinchmann J., Charlot S., Tremonti C., White S. D. M., 2004, ApJ, 613, 109
Holt J., Tadhunter C. N., Morganti R., Emonts B. H. C., 2011, MNRAS, 410, 1527
Hopkins P. F., Elvis M., 2010, MNRAS, 401, 7
Johansson P. H., Burkert A., Naab T., 2009, ApJ, 707, L184
Kim D.-C., Sanders D. B., 1998, ApJS, 119, 41
Kim D.-C., Veilleux S., Sanders D. B., 2002, ApJS, 143, 277
Lamastra A., Bianchi S., Matt G., Perola G. C., Barcons X., Carrera F. J., 2009, A&A, 504, 73
Lípari S., Terlevich R., Díaz R. J., Taniguchi Y., Zheng W., Tsvetanov Z., Carranza G., Dottori H., 2003, MNRAS, 340, 289
Liu G., Zakamska N. L., Greene J. E., Nesvadba N. P. H., Liu X., 2013, MNRAS, 436, 2576
McElroy R., Croom S. M., Pracy M., Sharp R., Ho I.-T., Medling A. M., 2015, MNRAS, 446, 2186
Morganti R., 2015, in Massaro F., Cheung C. C., Lopez E., Siemiginowska A., eds, IAU Symp. Vol. 313, Extragalactic Jets from Every Angle, Kluwer, Dordrecht, p. 283
Morganti R., Fogasy J., Paragi Z., Oosterloo T., Orienti M., 2013, Science, 341, 1082
Morganti R., Veilleux S., Oosterloo T., Teng S. H., Rupke D., 2016, A&A, 593, A30
Nagar N. M., Wilson A. S., Falcke H., Veilleux S., Maiolino R., 2003, A&A, 409, 115
Nesvadba N. P. H., Lehnert M. D., De Breuck C., Gilbert A. M., van Breugel W., 2008, A&A, 491, 407
Netzer H., Trakhtenbrot B., 2014, MNRAS, 438, 672
Osterbrock D. E., Ferland G. J., 2006, Astrophysics of Gaseous Nebulae and Active Galactic Nuclei, University Science Books, Sausalito, CA
Perna M. et al., 2015, A&A, 574, A82
Richings A. J., Faucher-Giguère C.-A., 2018, MNRAS, 474, 3673
Robinson T. G., Tadhunter C. N., Axon D. J., Robinson A., 2000, MNRAS, 317, 922

Rodríguez Zaurín J., Tadhunter C. N., González Delgado R. M., 2009, MNRAS, 400, 1139
Rodríguez Zaurín J., Tadhunter C. N., Rose M., Holt J., 2013, MNRAS, 432, 138
Rose M., Tadhunter C., Ramos Almeida C., Rodríguez Zaurín J., Santoro F., Spence R., 2018, MNRAS, 474, 128
Rupke D. S., Veilleux S., Sanders D. B., 2005, ApJ, 632, 751
Sanders D. B., Mirabel I. F., 1996, ARA&A, 34, 749
Schlafly E. F., Finkbeiner D. P., 2011, ApJ, 737, 103
Soifer B. T., Sanders D. B., Madore B. F., Neugebauer G., Danielson G. E., Elias J. H., Lonsdale C. J., Rice W. L., 1987, ApJ, 320, 238
Spence R. A. W., Zaurín J. R., Tadhunter C. N., Rose M., Cabrera-Lavers A., Spoon H., Muñoz-Tuñón C., 2016, MNRAS, 459, L16
Spoon H. W. W., Holt J., 2009, ApJ, 702, L42
Spoon H. W. W. et al., 2013, ApJ, 775, 127
Springel V., Di Matteo T., Hernquist L., 2005, MNRAS, 361, 776
Sun A.-L., Greene J. E., Zakamska N. L., 2017, ApJ, 835, 222
Surace J. A., Sanders D. B., Vacca W. D., Veilleux S., Mazzarella J. M., 1998, ApJ, 492, 116
Tadhunter C., Wills K., Morganti R., Oosterloo T., Dickson R., 2001, MNRAS, 327, 227
Tadhunter C., Morganti R., Rose M., Oonk J. B. R., Oosterloo T., 2014, Nature, 511, 440
Tadhunter C., Spence R., Rose M., Mullaney J., Crowther P., 2017, Nat. Astron., 1, 0061
Tadhunter C. et al., 2018, MNRAS, in press
Tombesi F., Meléndez M., Veilleux S., Reeves J. N., González-Alfonso E., Reynolds C. S., 2015, Nature, 519, 436
Veilleux S., Sanders D. B., Kim D.-C., 1997, ApJ, 484, 92
Veilleux S., Kim D.-C., Sanders D. B., 1999, ApJ, 522, 113
Veilleux S., Kim D.-C., Sanders D. B., 2002, ApJS, 143, 315
Veilleux S. et al., 2006, ApJ, 643, 707
Veilleux S. et al., 2013, ApJ, 776, 27
Veilleux S., Bolatto A., Tombesi F., Meléndez M., Sturm E., González-Alfonso E., Fischer J., Rupke D. S. N., 2017, ApJ, 843, 18
Villar-Martín M., Arribas S., Emonts B., Humphrey A., Tadhunter C., Bessiere P., Cabrera Lavers A., Ramos Almeida C., 2016, MNRAS, 460, 130
Yuan T.-T., Kewley L. J., Sanders D. B., 2010, ApJ, 709, 884
Zubovas K., 2018, MNRAS, 473, 3525
Zubovas K., King A. R., 2014, MNRAS, 439, 400

APPENDIX A: GENERAL DESCRIPTION OF TARGETS

In this section, we describe the general properties of the targets in our ULIRG sample.

F01004–2237: the single nucleus, compact morphology of this system suggests it is being observed at, or just after, the peak of the merger (Surace et al. 1998). Historically, it has been classified as both an HII galaxy and Seyfert 2 galaxy based on optical diagnostic line ratios: although the narrow components appear consistent with stellar photoionization, the broad components are more consistent with ionization by an AGN (Rodríguez Zaurín et al. 2013).

Interestingly, our new optical spectrum for this object shows that it has changed dramatically over the last decade – completely unexpectedly in the context of this study. Compared to previous spectra taken in 2005, the 2015 spectrum shows the appearance of unusually strong, broad helium emission lines (Tadhunter et al. 2017). A follow-up examination of an archival optical light-curve data revealed a significant flare in 2010, providing evidence for the first TDE ever observed in a starburst galaxy.

The [O III] profile was fit with three kinematic components: one narrow ($\Delta v = 63 \pm 25\,\mathrm{km\,s^{-1}}$; FWHM unresolved), one intermediate ($\Delta v = -361 \pm 35\,\mathrm{km\,s^{-1}}$; $\mathrm{FWHM} = 699 \pm 32\,\mathrm{km\,s^{-1}}$), and one broad ($\Delta v = -1045 \pm 60\,\mathrm{km\,s^{-1}}$; $\mathrm{FWHM} = 1586 \pm 38\,\mathrm{km\,s^{-1}}$). Note that, unlike the rest of the objects in this paper, whose host rest-frame redshifts were determined using stellar absorption features, the galaxy rest frame of F01004–2237 was determined using emission lines from extended quiescent gas either side of the nucleus, because any stellar absorption features that may have been present in the nuclear spectrum were washed out by the TDE continuum.

The red [O II] λ7325 trans-auroral blend is detected in the ground-based *WHT*/ISIS spectrum, however the blue [SII] λ4072 blend is washed out by emission lines associated with the TDE. Fortunately, the latter blend is detectable in the *HST*/STIS spectrum, from which an estimate of the total emission-line flux has been obtained.

Based on the STIS spectroscopy, F01004–2237 shows evidence for a compact ($R_{[\mathrm{O\,III}]} = 0.111 \pm 0.004\,\mathrm{kpc}$) ionized nuclear outflow, consistent with the upper limit of 1.1 kpc derived from the ground-based spectrum. Using $\log n_\mathrm{e}\ (\mathrm{cm^{-3}}) = 4.00^{+0.25}_{-0.30}$ and $E(B-V) = 0.04 \pm 0.16$, we calculate a mass outflow rate for the maximal velocity case of $1.0^{+2.2}_{-0.8}\ \mathrm{M_\odot\ yr^{-1}}$. We find the kinetic power of this outflow corresponds to be $0.14^{+0.35}_{-0.10}$ per cent L_bol.

F05189–2524: the closest ULIRG considered in the paper ($z = 0.0428$), F05189–2524 was not part of the original QUADROS sample, although it fulfils the redshift and spectral selection criteria of that sample; it was observed to fill a gap in the schedule during the observing run. F05189–2524 is a late-stage merger surrounded by tidal debris (Veilleux et al. 2002, 2006). In *HST* images, it shows a complex nuclear structure, dominated by two bright knots separated by ∼0.25 arcsec (Surace et al. 1998). It is not yet clear whether these two knots represent a true double nucleus, or a single nucleus bisected by a dust lane; however, the *HST*/STIS long-slit spectrum – which cuts through both knots – shows that the AGN is associated with the more northerly of the two knots. The extraction aperture for the ground-based optical spectrum, presented in Fig. 1, includes both of the bright near-nuclear knots and shows strong Balmer absorption features, as well as emission lines with a wide range of ionization, including strong [Nev] and [Fe VII] lines. An in-depth study of the high-ionization, coronal line outflow detected in the *HST*/STIS spectrum of this object will be presented in Rose et. al (in preparation).

The emission-line profile of [OIII] is shown in Fig. 4. Notably, there is no rest-frame [O III] component detected within our *WHT*/ISIS slit. The entire profile is significantly blueshifted with respect to the host galaxy rest frame, consistent with Rupke et al. (2005), with the best-fitting model requiring two Gaussian components: an intermediate component with $\Delta v = -505 \pm 26\,\mathrm{km\,s^{-1}}$ and $\mathrm{FWHM} = 582 \pm 37\ \mathrm{km\,s^{-1}}$, and a broad component with $\Delta v = -1072 \pm 44\ \mathrm{km\,s^{-1}}$ and $\mathrm{FWHM} = 1706 \pm 24\ \mathrm{km\,s^{-1}}$. In contrast, an additional intermediate component is detected in the Balmer emission lines with $\Delta v = -28 \pm 55\ \mathrm{km\,s^{-1}}$ and $\mathrm{FWHM} = 555 \pm 76\ \mathrm{km\,s^{-1}}$, consistent with the host rest frame.

The high-critical-density trans-auroral [S II] and [O II] blends are barely detected in the *WHT*/ISIS spectrum, but are detected in the *HST*/STIS spectrum. The kinematic models (relative shifts and widths of the components) fitted to the emission lines in the *WHT*/ISIS spectrum also fitted well to the *HST*/STIS profiles. Therefore, we were able to use the trans-auroral ratios from this spectrum to estimate the density and reddening of the warm outflow.

Based on the STIS long-slit spectroscopy, F05189–2524 shows evidence for a compact ($R_{[\mathrm{O\,III}]} = 0.079 \pm 0.002\,\mathrm{kpc}$) ionized nuclear outflow, which is consistent with the 0.3 kpc upper limit derived from the ground-based spectrum. F05189–2524 has the highest estimated density, $\log n_\mathrm{e}\ (\mathrm{cm^{-3}}) = 4.25 \pm 0.25$,

of all the ULIRGs considered in this paper. Combined with $E(B-V) = 0.02 \pm 0.15$, this corresponds to a modest mass outflow rate and kinematic power (maximal velocity case: $\dot{M} = 0.13^{+0.21}_{-0.09}$ $M_\odot$ yr^{-1}; $\log(\dot{E}) = 40.3 \pm 0.4$ erg s^{-1} $= (2.6^{+4.9}_{-1.8}) \times 10^{-2}$ per cent L_{bol}).

Previous evidence for warm ionized outflows via broad, blueshifted kinematics was reported by Arribas et al. (2014) based on fits to the [N II]+Hα blend. This object also shows blueshifted kinematics in OH 119 μm observations (Veilleux et al. 2013), and outflow signatures are detected in the neutral gas based on Na ID absorption-line observations (Rupke et al. 2005). Rupke et al. (2005) estimate a neutral gas mass outflow rate $\dot{M} = 117\,M_\odot$ yr^{-1} and kinetic power $\log(\dot{E}) = 43.08$ erg s^{-1} – orders of magnitude higher than the mass outflow rate and kinetic power we derive for the warm ionized gas in this study.

F14394+5332E: this object consists of two interacting galaxies separated by ∼56 kpc and connected by a bridge of faint, diffuse emission (Kim, Veilleux & Sanders 2002; Tadhunter et al. 2018). The spectroscopic slit for our *WHT*/ISIS observations was placed on the more westerly of the two nuclei in the eastern galaxy (Kim et al. 2002) that contains the optical AGN nucleus, and for which a powerful ionized nuclear outflow has been previously reported in Rodríguez Zaurín et al. (2013), based on the [O III] emission lines (see also Lípari et al. 2003). Evidence for a molecular outflow is also reported in Veilleux et al. (2013), based on blueshifted OH 119μm profiles. Our total trans-auroral flux ratio and Balmer decrement measurements both indicate a moderate degree of intrinsic reddening for the warm outflow in this object ($E(B-V) \sim 0.6$).

The [O III] emission-line profile is spectacular. The best fit requires three narrow components (N1: $\Delta v = 17 \pm 62$ km s^{-1}; FWHM $= 408 \pm 11$ km s^{-1}; N2: $\Delta v = -701 \pm 63$ km s^{-1}; FWHM $= 288 \pm 21$ km s^{-1}; and N3: $\Delta v = -1457 \pm 66$ km s^{-1}; FWHM $= 242 \pm 34$ km s^{-1}) and one broad component ($\Delta v = -1000 \pm 67$ km s^{-1}; FWHM $= 1871 \pm 19$ km s^{-1}). These velocity shifts are given relative to the host galaxy rest frame, as measured from the higher order Balmer absorption lines.

Given that the two blueshifted narrow components of [O III] were not detected in any of the other emission lines, an alternative three-component model was created from the red [S II] $\lambda\lambda$6717,6731 blend (N: $\Delta v = 17 \pm 63$ km s^{-1}; FWHM $= 420 \pm 11$ km s^{-1}; I: $\Delta v = -358 \pm 93$ km s^{-1}; FWHM $= 986 \pm 42$ km s^{-1}; and B: $\Delta v = -1030 \pm 69$ km s^{-1}; FWHM $= 1927 \pm 20$ km s^{-1}).

Based on our ground-based analysis, F14394+5332E shows evidence for a resolved ionized outflow with a radius of 0.75 ± 0.12 kpc. In comparison, the radius estimated from the flux-weighted mean of the *HST*/ACS imaging is 0.840 ± 0.008 kpc (Tadhunter et al. 2018). The consistency between these two independent methods is remarkable, given the different techniques involved. The estimated density based on the total trans-auroral flux ratios is $\log n_e$ (cm^{-3}) $= 2.90^{+0.30}_{-0.40}$; however, this increases to $\log n_e$ (cm^{-3}) $= 3.55^{+0.45}_{-0.45}$ when considering only the broad, outflowing component. The narrow component of the trans-auroral lines give a density of $\log n_e$ (cm^{-3}) $= 2.70^{+0.35}_{-0.50}$.

We can also place an upper limit on the density of the narrow kinematic component based on a fit to the traditional [S II] $\lambda\lambda$6717,6731 of $\log n_e$ (cm^{-3}) < 2.64, which is consistent within the errors with the trans-auroral estimate. Interestingly, the intermediate component of the kinematic fit to the traditional [S II] emission gives a density of $\log n_e$ (cm^{-3}) $= 3.05^{+0.21}_{-0.19}$, illustrating the density gradient between the narrow, rest-frame component and broad, outflowing component of the gas.

In the maximal velocity case, for $E(B-V) = 0.63^{+0.22}_{-0.30}$, the trans-auroral broad-component density leads to a mass outflow rate, $\dot{M} = 3.4^{+13.8}_{-3.0}$ $M_\odot$ yr^{-1} and kinetic power, $\dot{E}/L_{bol} = 0.66^{+3.12}_{-0.60}$ per cent.

F17044+6720: this is a highly disturbed system, with two bright nuclear continuum condensations, a prominent series of dust features and a ∼15 kpc tidal tail to the north (Tadhunter et al. 2018). The extraction aperture for our *WHT*/ISIS observations was centred on the brightest nuclear continuum condensation, which also contains the AGN nucleus and warm outflow.

Despite the disturbed morphology, the [O III] emission-line profile is one of the least disturbed of the eight ULIRGs in the paper, with a strong, narrow rest-frame component ($\Delta v = -1.2 \pm 61$ km s^{-1}; FWHM $= 218 \pm 12$ km s^{-1}) and a weaker, blueshifted broad component associated with the outflow ($\Delta v = -503 \pm 85$ km s^{-1}; FWHM $= 1757 \pm 60$ km s^{-1}). The [O III] kinematic model provided a good fit to all other emission lines.

Based on our ground-based analysis, F17044+6720 shows the most extended ionized outflow out of the eight ULIRGs considered in this paper, with an estimated radius of 1.45 ± 0.18 kpc. Similarly to F14394+5332E, we can compare this with the flux-weighted mean estimate from the *HST*/ACS [OIII] imaging from Tadhunter et al. (2018), which is given as 1.184 ± 0.006 kpc. The two estimates are consistent to within 2σ of the joint error.

The density derived from the total trans-auroral emission-line ratios is $\log n_e$ (cm^{-3}) $= 2.50^{+0.30}_{-0.50}$ – the lowest density estimated using this technique for any of the objects in this paper; however, the broad component to the trans-auroral lines is extremely weak in this case, therefore the total trans-auroral fluxes are likely dominated by the narrow component, for which a lower density would be expected. Indeed, the density derived using the traditional [SII] $\lambda\lambda$6717,6731 emission-line ratio for the narrow components is consistent with this, giving an estimated density of $\log n_e$ (cm^{-3}) $= 2.49^{+0.15}_{-0.18}$.

The mass outflow rate and kinetic power estimates based on the density obtained from the total trans-auroral flux ratios, with $E(B-V) = 0.35 \pm 0.10$, remain relatively modest despite the low density. For the maximal velocity case, we find $\dot{M} = 1.2^{+3.8}_{-0.8}$ $M_\odot$ yr^{-1} and $\dot{E}/L_{bol} = 0.42^{+1.69}_{-0.30}$ per cent.

F17179+5444: although the continuum morphology of this single-nucleus object is complex due to a series of dust features that cross the nuclear regions, its [OIII] emission is dominated by a compact region associated with the brightest nuclear continuum condensation (Tadhunter et al. 2018); the spectroscopic extraction aperture for our *WHT*/ISIS observations was centred on this region. While evidence for warm ionized outflows from [OIII] emission] is reported in Rodríguez Zaurín et al. (2013), Rupke et al. (2005) found no evidence for significant outflows using the Na ID absorption lines.

F17179+5444 is one of two objects in our sample that can be considered radio loud, with $L_{1.4GHz} = 10^{25.23}$ W Hz^{-1}. To date, however, there have been no reports of jets associated with this radio emission. Our total trans-auroral flux and Balmer diagnostics indicate moderate-to-high dust extinction in this object, with $E(B-V) \sim 0.7$.

The [O III] emission-line profile has been fit with two components: one rest-frame component, labelled intermediate using our FWHM criteria ($\Delta v = 58 \pm 62$ km s^{-1}; FWHM $= 590 \pm 12$ km s^{-1}), and one blueshifted broad component ($\Delta v = 242 \pm 78$ km s^{-1}; FWHM $= 1530 \pm 33$ km s^{-1}). Note, however, that Rodríguez Zaurín et al. (2013) fitted this profile with three components, splitting the intermediate component into two narrow components and suggesting that this splitting could be due to unresolved rotation.

The [O III] kinematic model worked well for the H β, [N II]+H α, and [O II] emission lines, however it failed to successfully fit the [S II] blends. For these, an alternative two component model was fitted to the red [S II] $\lambda\lambda$6717,6731 blend, where the relative widths and shifts of the broad components were allowed to vary with respect to the [O III] model to produce an acceptable fit. However, the broad component to the blue [S II] $\lambda\lambda$4068,4076 blend was not detected and only required the narrow component, consistent with the narrow component of the [O III] model.

Based on our analysis, F17179+5444 shows evidence for a compact ionized nuclear outflow. The outflow is unresolved in our ground-based observations, and we therefore derive an upper limit on the radius of 1.0 kpc. This is consistent with the estimate of $r = 0.112 \pm 0.007$ kpc for the compact [O III] nucleus from Tadhunter et al. (2018).

The density we derive from the total trans-auroral lines flux ratios is log n_e (cm^{-3}) = $3.05^{+0.30}_{-0.45}$. However, because the broad component of the blue [S II] blend was not detected, this is likely to be dominated by the narrow emission, leading to an underestimate of the true outflow density. Based on this density, and $E(B-V) = 0.70 \pm 0.15$, for the maximal velocity case we estimate a mass outflow rate, $\dot{M} = 20.1^{+72.9}_{-14.9}$ M$_\odot$ yr^{-1} and kinetic power, $\dot{E}/L_{\rm bol} = 2.5^{+10.7}_{-1.9}$ per cent. The latter are the highest values measured for any object in the QUADROS sample; however, this may be a consequence of the fact that the densities have been underestimated using the total trans-auroral flux ratios.

F23060+0505: this object hosts the most powerful AGN out of the eight ULIRGs in this paper, with its estimated bolometric luminosity of 4.6×10^{45} erg s^{-1} placing it in the quasar category. Kim et al. (2002) showed it to be a single-nucleus system with a diffuse tidal feature to the south-west. Our total trans-auroral flux and Balmer decrement diagnostic measurements for the extracted nuclear spectra indicate a moderate degree of intrinsic reddening ($E(B-V) \sim 0.5$) for the outflowing warm gas. Cicone et al. (2014) report evidence for a massive molecular outflow in this object, based on CO emission. Although they put an upper limit on the mass outflow rate of 1500 M$_\odot$ yr^{-1}, they note that the observations did not fully qualify as an outflow detection based on their criteria.

Despite the classification of this object as a type 2 object based on its optical spectrum, the steep rise in the continuum at the red end of the optical spectrum, and the detection of broad components (>2000 km s^{-1}) to both the H α and Pa α emission lines, indicate the presence of a moderately reddened type 1 AGN component (Veilleux et al. 1999; Rodríguez Zaurín et al. 2013, this paper). Indeed, the [N II]+H α blend in our spectrum required a VB component to H α (FWHM = 2359 $\pm$ 69 km s^{-1}) for an acceptable fit.

A four-component model was required to fit the [O III] profile: two narrow (N1: $\Delta v = 273 \pm 34$ km s^{-1}; FWHM = 147 $\pm$ 37 km s^{-1}, and N2: $\Delta v = -25 \pm 38$ km s^{-1}; FWHM = 267 $\pm$ 35 km s^{-1}), one intermediate ($\Delta v = -283 \pm 44$ km s^{-1}; FWHM = 934 $\pm$ 32 km s^{-1}), and one broad component ($\Delta v = -1220 \pm 146$ km s^{-1}; FWHM = 1399 $\pm$ 114 km s^{-1}). The [O III] model did not successfully fit the [O II] and [S II] blends. For these, a three-component model based on [O II]3727 was used.

Based on our analysis, F23060+0505 hosts an ionized outflow with a radius of 1.41 $\pm$ 0.19 kpc. No other radius estimates are available for comparison this object; however, given to the consistency between the different methods used for the other objects considered in this paper, we are confident in this value.

The density we calculate based on the total trans-auroral emission-line ratios is log n_e (cm^{-3}) = $3.10^{+0.35}_{-0.50}$. However, similarly to F17179+5444, the broad component of the blue [S II] $\lambda\lambda$4068,4076 blend was not detected, meaning this density is likely to be an underestimate for the outflow region. Despite this, for the maximal velocity case and $E(B-V) = 0.45^{+0.15}_{-0.20}$, we estimate a relatively low mass outflow rate ($\dot{M} = 2.2^{+8.1}_{-1.7}$ M$_\odot$ yr^{-1})m and ratio of kinetic power to bolometric luminosity ($\dot{E}/L_{\rm bol} = (2.7^{+13.2}_{-2.2}) \times 10^{-2}$ per cent). Despite claims of a massive molecular outflow in this object, the outflow in the ionized phase appears modest.

F23233+2817: Kim et al. (2002) and Veilleux et al. (2002) shows this source to have spiral-like morphology surrounding a very compact nucleus, with no visible tidal tails. They note that this is the only object in the original 1 Jy sample with no obvious sign of interaction. Evidence for molecular outflows in this source, based on the OH 119 μm feature, is presented in Veilleux et al. (2013). Our trans-auroral and Balmer diagnostics indicate low intrinsic reddening for the source ($E(B-V) \sim 0.2$) in the extracted nuclear spectrum.

The [O III] profile requires a three component model: one narrow component ($\Delta v = -92 \pm 27$ km s^{-1}; FWHM = 239 $\pm$ 21 km s^{-1}), one intermediate component ($\Delta v = -316 \pm 31$ km s^{-1}; FWHM = 760 $\pm$ 13 km s^{-1}), and one broad component ($\Delta v = -785 \pm 54$ km s^{-1}; FWHM = 1892 $\pm$ 40 km s^{-1}). This model was successful in fitting the other emission lines; however, no broad component was detected in the [S II] blends.

Based on our analysis, F23233+2817 shows evidence for a relatively compact ionized outflow. The outflow is unresolved compared to the seeing, so we place an upper limit on the radius of 1.1 kpc. The density we obtain from the total trans-auroral emission-line ratios is log n_e (cm^{-3}) = $3.10^{+0.30}_{-0.40}$. This, however, is likely to be dominated by the low-density narrow component due to the broad component of the [S II] blends being undetected. Nevertheless, based on this density, $E(B-V) = 0.15 \pm 0.15$ and the maximal velocity assumptions, we obtain lower limits on the mass outflow rate and kinetic powers of $\dot{M} > 0.11$ M$_\odot$ yr^{-1} and $\dot{E}/L_{\rm bol} > 9.5 \times 10^{-2}$ per cent.

F23389+0303N: this is the most extreme source of the eight ULIRGs in terms of its [OIII] kinematics and trans-auroral ratios. Described as a close binary, separated by 5.2 kpc, by Kim et al. (2002) and Veilleux et al. (2002), with a short tidal feature to the south, our spectroscopic extraction aperture was centred on the northern nucleus of the system. Evidence for blueshifted kinematics has been reported for neutral Na ID and molecular OH 119 μm in Rupke et al. (2005) and Veilleux et al. (2013) respectively. Rupke et al. (2005) place a lower limit on the neutral mass outflow rate of $\dot{M} > 49$ M$_\odot$ yr^{-1}, and the kinetic power $\dot{E} > 10^{42.39}$ erg s^{-1}. Along with F17179+5444, F23389+0303N is one of two objects in this paper which are radio loud ($L_{1.4\rm GHz} = 10^{25.63}$ W Hz^{-1}). A radio map of this object is presented in Nagar et al. (2003), that shows two slightly resolved radio lobes separated by ~830 pc.

The most striking features of the spectrum of this source, are the strengths and breadths of the [O I] λ6300 and trans-auroral [O II] λ7325 emission features, which are stronger than the broad components to the [OIII] emission lines. It is very unusual to see such relative emission-line strengths between these species. The great strength of the high-critical-density trans-auroral [OII] blend immediately suggests that we are sampling high-density gas.

The [O III] profile is very broad, requiring two components for an acceptable fit: one narrow ($\Delta v = -191 \pm 27$ km s^{-1}; FWHM = 402 $\pm$ 16 km s^{-1}) and one very broad ($\Delta v = -134 \pm 36$ km s^{-1}; FWHM = 2346 $\pm$ 38 km s^{-1}). Both components are

blueshifted relative to the stellar rest frame, however the very broad component, which dominates the flux, is slightly redshifted with respect to the narrow component. This kinematic model was successful at fitting all the other diagnostic emission lines, as illustrated in Fig. 5.

Our analysis indicates F23389+0303N contains one of the highest density outflows of the QUADROS sample, with the broad trans-auroral ratios leading to $\log n_e\ (\mathrm{cm}^{-3}) = 4.20 \pm 0.10$. It is also a highly reddened object, with $E(B-V) \sim 1$. The outflow region is unresolved in our ground-based observations, and we place an upper limit on the radius of 1.2 kpc. However if we assume the outflow is jet-driven (see Batcheldor et al. 2007; Tadhunter et al. 2014, for example), we can use the radius of the radio lobes, $r = 0.415$ kpc (Nagar et al. 2003) as a proxy for the radius of the warm outflow. This estimate, combined with the density derived from the broad trans-auroral component and $E(B-V) = 0.90 \pm 0.05$, leads to $\dot{M} = 10.4^{+11.1}_{-5.1}\ \mathrm{M}_\odot\ \mathrm{yr}^{-1}$ and $\dot{E} = 10^{43.2 \pm 0.3}\ \mathrm{erg\,s}^{-1} = 0.63^{+0.79}_{-0.33}$ per cent L_{bol} for the maximal velocity case.

This paper has been typeset from a TEX/LATEX file prepared by the author.